PITT-PACC 1402

Determining the Dark Matter Particle Mass through Antler Topology Processes at Lepton Colliders

Neil D. Christensen[1,2], Tao Han[2,3], Zhuoni Qian[2],
Josh Sayre[2], Jeonghyeon Song[4], and Stefanus[2]

[1] *Department of Physics, Illinois State University, Normal, IL 61790 USA*

[2] *Pittsburgh Particle physics Astrophysics and Cosmology Center, Department of Physics and Astronomy, University of Pittsburgh, Pittsburgh, PA 15260 USA*

[3] *Korea Institute for Advanced Study, Seoul 130-722, Korea*

[4] *Division of Quantum Phases & Devices, School of Physics, KonKuk University, Seoul 143-701, Korea*

arXiv:1404.6258v2 [hep-ph] 30 Oct 2014

Abstract

We study the kinematic cusps and endpoints of processes with the "antler topology" as a way to measure the masses of the parity-odd missing particle and the intermediate parent at a high energy lepton collider. The fixed center of mass energy at a lepton collider makes many new physics processes suitable for the study of the antler decay topology. It also provides new kinematic observables with cusp structures, optimal for the missing mass determination. We also study realistic effects on these observables, including initial state radiation, beamstrahlung, acceptance cuts, and detector resolution. We find that the new observables, such as the reconstructed invariant mass of invisible particles and the summed energy of the observable final state particles, appear to be more stable than the commonly considered energy endpoints against realistic factors and are very efficient at measuring the missing particle mass. For the sake of illustration, we study smuon pair production and chargino pair production within the framework of the minimal supersymmetric standard model. We adopt the log-likelihood method to optimize the analysis. We find that at the 500 GeV ILC, a precision of approximately 0.5 GeV can be achieved in the case of smuon production with a leptonic final state, and approximately 2 GeV in the case of chargino production with a hadronic final state.

PACS numbers: 13.85.Rm, 13.66.Hk

I. INTRODUCTION

With the monumental discovery of the Higgs boson at the LHC [1], all of the fundamental particles in the standard model (SM) have been discovered. The SM as an effective field theory can be valid up to a very high scale. Nevertheless, there are strong indications that the SM is incomplete. Certain observed particle physics phenomena cannot be accounted for within the SM. Among them, the discovery and characterization of the dark matter (DM) particle may be one of the most pressing issues.

The existence of dark matter has been well established through a combination of galactic velocity rotation curves [2], the cosmic microwave background [3], Big Bang nucleosynthesis [4], gravitational lensing [5], and the bullet cluster [6]. As a result of these observations, we know that dark matter is non-baryonic, electrically neutral and composes roughly 23% of the energy and 83% of the matter of the universe.

Among the many possibilities for dark matter [7], weakly interacting massive particles (WIMPs) are arguably the most attractive because of the so-called WIMP miracle: to get the relic abundance right, a WIMP mass is roughly

$$M_{\rm WIMP} \lesssim \frac{g^2}{0.3}\ 1.8\ {\rm TeV}, \tag{1}$$

which miraculously coincides with the new physics scale expected from the "naturalness" argument for electroweak physics. Therefore, there is a high hope that the search for a dark matter particle may be intimately related to the discovery of TeV scale new physics.

Direct searches of weak scattering of dark matter off nuclear targets in underground labs have been making great progress in improving the sensitivity to the DM mass and couplings, most recently by the XENON [8], LUX [9] and SuperCDMS [10] collaborations. WIMPs can also be produced at colliders either directly in pairs or from cascade decays of other heavier particles. Since a WIMP is non-baryonic and electrically neutral, it does not leave any trace in the detectors and thus only appears as missing energy. In order to establish a DM candidate convincingly, it is ultimately important to reach consistency between direct searches and collider signals for the common parameters of mass, spin and coupling strength.

It is very challenging to determine the missing particle mass at colliders due to the underconstrained kinematical system with two missing particles in an event. It is particularly difficult at hadron colliders because of the unknown partonic c.m. energy and frame. There

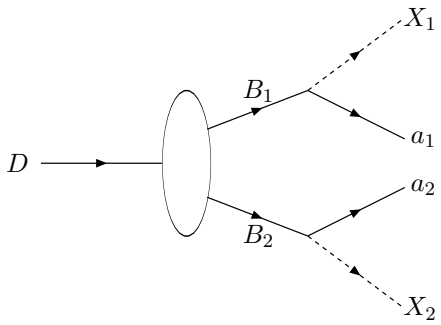

FIG. 1: The antler decay diagram of a heavy particle D into two visible particles a_1 and a_2 and two invisible particles X_1 and X_2 through on-shell intermediate particles B_1 and B_2.

exist many attempts to determine the missing particle mass at the LHC, such as endpoint methods [11], polynomial methods [12], M_{T2} methods [13], and the matrix element method [14]. Recently, we studied the "antler decay" diagram [15], as illustrated in Fig. 1 with a resonant decay of a heavy particle D into two parity-odd particles (B_1 and B_2) at the first step, followed by each B_i's decay into a missing particle X_i and a visible particle a_i. We found that a resonant decay through the antler diagram develops cusps in some kinematic distributions and the cusp positions along with the endpoint positions determine the missing particle mass as well as the intermediate particle mass [15–17].

In this article, we focus on lepton colliders [18–21], in which the antler topology applies. The initial state is well-defined with fixed c.m. energy and c.m. frame. This allows various antler processes without going through a resonant decay of a heavy particle D. We consider kinematic variables such as the angle and the energy of a visible particle for the mass determination. We also show that the invariant mass of two invisible particles, which can be indirectly reconstructed using the recoil mass technique, is crucial for the mass measurement and the SM background suppression. The energy sum of the two visible particles or of the two invisible particles will also be shown to be equally powerful. At a linear e^+e^- collider, the available beam polarization can additionally be used to suppress the SM background and enhance the sensitivity of the mass measurement.

Two common methods of the missing mass measurement have been studied in the literature for e^+e^- collisions:

1. The lepton energy endpoints in cascade decays [22];

2. The photon energy endpoint in the direct WIMP pair production associated with a photon [23].

In comparison, we find that our results from the antler topology can be at least comparable to the energy endpoint method and do much better than the single photon approach. For the sake of illustration, we will concentrate on the minimal supersymmetric standard model (MSSM) and consider the scenario where the lightest neutralino $\tilde{\chi}_1^0$ is the lightest supersymmetric particle (LSP) and, therefore, stable in the framework of a R-parity conserving scenario. We consider two MSSM processes that satisfy the antler topology: pair production of scalar muons (smuons) and that of charginos. In order to be as realistic as possible with the kinematical construction, we analyze the effects of the initial state radiation (ISR), beamstrahlung, acceptance cuts, and detector resolutions on the observables. We adopt the log-likelihood method based on Poisson statistics to quantify the precision of the mass measurements. We find that this method optimizes the sensitivity to the mass parameters in the presence of these realistic effects.

We note that the scanning through the pair production threshold could give a much more accurate determination for the intermediate parent mass [24]. With this as an input, one could improve the measurement of the missing particle mass by the energy endpoint method or by the Antler technique. However, the threshold scan would require *a priori* knowledge of the intermediate particle mass, and would need more integrated luminosity to reach such a high sensitivity [24]. Our proposed method does not assume to know any masses, and our outputs would benefit the design of the threshold scan.

The rest of the paper is organized as follows. In section II, we review the kinematic cusps and endpoints of antler processes. We present the analytic expressions for six kinematic variables in terms of the masses. For a benchmark scenario, we first show smuon pair production as an example of massless visible particles in section III. We reproduce the expected kinematical features numerically and illustrate the effects of the acceptance cuts on the final state observable particles. Other realistic effects including full spin correlation, SM backgrounds, ISR, beamstrahlung, and detector resolutions are considered. Adopting the log-likelihood method based on the Poisson probability density, we quantify the accuracy with which the missing particle mass measurement may be determined in section III D. In section IV, chargino pair production is studied, as an example of massive visible particles with a hadronic final state. In section V, we give a summary and draw our conclusions.

	$\mathcal{R}_1:\ \eta_B < \frac{\eta_a}{2}$	$\mathcal{R}_2:\ \frac{\eta_a}{2} < \eta_B < \eta_a$	$\mathcal{R}_3:\ \eta_a < \eta_B$
$m_{aa}^{\rm min}$	$2m_a$		$2m_a \cosh(\eta_B - \eta_a)$
$m_{aa}^{\rm cusp}$	$2m_a \cosh(\eta_B - \eta_a)$	$2m_a \cosh\eta_B$	
$m_{aa}^{\rm max}$	$2m_a \cosh(\eta_B + \eta_a)$		

TABLE I: The cusp and endpoints of the invariant mass distribution m_{aa} in the three regions of c.m. energy and parameter space.

II. CUSPS AND ENDPOINTS OF THE ANTLER PROCESS

We start from a state with a fixed c.m. energy $\sqrt{s}$, which produces two massive particles B_1 and B_2, followed by each B's decay into a visible particle a and an invisible heavy particle X, as depicted in Fig. 1. In e^+e^- collisions, it is realized as

$$\begin{aligned} e^+e^- \ &\to\ B_1 + B_2, \\ &\qquad B_1 \to a_1 + X_1, \quad B_2 \to a_2 + X_2. \end{aligned} \tag{2}$$

For simplicity, we further assume that B_1 and B_2 (X_1 and X_2) are identical particles to each other:

$$m_{B_1} = m_{B_2} \equiv m_B, \quad m_{X_1} = m_{X_2} = m_X. \tag{3}$$

The kinematics is conveniently expressed by the rapiditiies η_j (equivalent to the speed $\beta = |\vec{p}|/E$), which specifies the four-momentum of a massive particle j from a two-body decay of $i \to j + k$ in the rest frame of the parent particle i as $p_j^{(i)} = m_j \left(\cosh\eta_j,\ \hat{p}_j^{(i)} \sinh\eta_j\right)$. In general, the kinematics of Eq.(2) is determined by three rapidities of the intermediate particle B, the visible particle a, and the missing particle X, given by

$$\cosh\eta_B = \frac{\sqrt{s}}{2m_B}, \quad \cosh\eta_a = \frac{m_B^2 - m_X^2 + m_a^2}{2m_a m_B}, \quad \cosh\eta_X = \frac{m_B^2 - m_W^2 + m_X^2}{2m_X m_B}. \tag{4}$$

Note that in the massless visible particle case ($m_a = 0$) the rapidity η_a goes to infinity.

We find the distributions of the following six kinematic variables informative:

$$m_{aa}, \quad m_{\rm rec}, \quad \cos\Theta, \quad E_a, \quad E_{aa}, \quad E_{XX}. \tag{5}$$

(i) m_{aa} *distribution*: m_{aa} is the invariant mass of the two visible particles. This distribution accommodates three singular points: a minimum, a cusp, and a maximum. Their positions

are not uniquely determined by the involved masses. They differ according to the relative scales of masses. There are three regions [16]

$$\mathcal{R}_1 : \eta_B < \frac{\eta_a}{2}, \quad \mathcal{R}_2 : \frac{\eta_a}{2} < \eta_B < \eta_a, \quad \mathcal{R}_3 : \eta_a < \eta_B. \tag{6}$$

The cusps and endpoints in the three regions are given in Table I. The minimum endpoint is the same for $\mathcal{R}_1$ and $\mathcal{R}_2$ but different for $\mathcal{R}_3$. The cusp is the same for $\mathcal{R}_2$ and $\mathcal{R}_3$, which is different for $\mathcal{R}_1$. The maximum endpoints are the same for all three regions. The absence of *a priori* knowledge of the masses gives us ambiguity among $\mathcal{R}_1$, $\mathcal{R}_2$, and $\mathcal{R}_3$. For example we do not know whether the measured $m_{aa}^{\rm min}$ is $2m_a$ or $2m_a \cosh(\eta_B - \eta_a)$.

In the massless visible particle case, however, three singular positions are uniquely determined as

$$\begin{aligned} m_{aa}^{\rm min} &= 0\,, \\ m_{aa}^{\rm cusp} &= m_B \left(1 - \frac{m_X^2}{m_B^2}\right) e^{-\eta_B}\,, \\ m_{aa}^{\rm max} &= m_B \left(1 - \frac{m_X^2}{m_B^2}\right) e^{\eta_B}\,. \end{aligned} \tag{7}$$

According to the analytic function for the m_{aa} distribution [15], the m_{aa} cusp is sharp only when the B pair production is near threshold, *i.e.*, when $0.443\sqrt{s} < m_B < 0.5\sqrt{s}$.

(*ii*) $m_{\rm rec}$ *distribution*: The invariant mass of two invisible particles, denoted by $m_{\rm rec}$, can be measured through the relation

$$m_{\rm rec}^2 \equiv m_{XX}^2 = s - 2\sqrt{s}\,(E_{a_1} + E_{a_2}) + m_{aa}^2. \tag{8}$$

The $m_{\rm rec}$ distribution is related to the invariant mass distribution of massive visible particles because of the symmetry of the antler decay topology. It also has three singular points, $m_{\rm rec}^{\rm min}$, $m_{\rm rec}^{\rm cusp}$, and $m_{\rm rec}^{\rm max}$. Their positions are as in Table I, with replacement of $m_a \to m_X$ and $\eta_a \to \eta_X$.

(*iii*) E_a *distribution*: The energy distribution of one visible particle in the lab frame also provides important information about the masses. If the intermediate particle B is a scalar particle like a slepton, its decay is isotropic and thus produces a flat rectangular distribution. Two end points, $E_a^{\rm min}$ and $E_a^{\rm max}$, are determined by the masses:

$$E_a^{\rm max,min} = \frac{\sqrt{s}}{4}\left(1 - \frac{m_X^2 - m_a^2}{m_B^2}\right)\left(1 \pm \beta_B \sqrt{1 - \frac{4m_a^2 m_B^2}{(m_B^2 + m_a^2 - m_X^2)^2}}\right), \tag{9}$$

where β_B is defined by

$$\beta_B = \sqrt{1 - \frac{4m_B^2}{s}}. \tag{10}$$

Note that if $m_B \ll \sqrt{s}/2$ or $m_X \approx m_B$, then $E_a^{\rm min}$ can be very small, even below the experimental acceptance for observation.

(*iv*) E_{aa} *distribution*: The distribution of the combined energy of the a_1a_2 system, $E_{aa} \equiv E_{a_1} + E_{a_2}$, is triangular, leading to three singular positions, $E_{aa}^{\rm min}$, $E_{aa}^{\rm cusp}$, and $E_{aa}^{\rm max}$, which are in terms of masses

$$\begin{aligned} E_{aa}^{\rm max,mix} &= 2m_a \cosh(\eta_a \pm \eta_B), \\ E_{aa}^{\rm cusp} &= 2m_a \cosh\eta_a \cosh\eta_B. \end{aligned} \tag{11}$$

For $m_a = 0$, we have simpler expressions as

$$\begin{aligned} E_{aa}^{\rm max,mix}\big|_{m_a=0} &= \frac{\sqrt{s}}{2}\left(1 - \frac{m_X^2}{m_B^2}\right)(1 \pm \beta_B), \\ E_{aa}^{\rm cusp}\big|_{m_a=0} &= \frac{\sqrt{s}}{2}\left(1 - \frac{m_X^2}{m_B^2}\right). \end{aligned} \tag{12}$$

(*v*) E_{XX} *distribution*: Although the energy of one invisible particle is not possible to measure, the sum of two invisible particle energies can be measured through

$$E_{XX} \equiv E_{X_1} + E_{X_2} = \sqrt{s} - E_{aa}. \tag{13}$$

The distribution of E_{XX} is a mirror image of the E_{aa} distribution, which is triangular with a sharp cusp.

(*vi*) $\cos\Theta$ *distribution*: Here Θ is the angle between the momentum direction of one visible particle (say a_1) in the c.m. frame of a_1 and a_2 and the c.m. moving direction of the pair in the lab frame. For $m_a \neq 0$, the $\cos\Theta$ distribution does not present a sharp cusp or endpoint [16]. If $m_a = 0$, however, the distribution has a simple functional form as

$$\left.\frac{d\Gamma}{d\cos\Theta}\right|_{m_a=0} \propto \begin{cases} \dfrac{1}{\sin^3\Theta}, & \text{for } |\cos\Theta| < \beta_B, \\ 0, & \text{otherwise}, \end{cases} \tag{14}$$

which accommodates two pronounced peaks where the cusp and the maximum endpoint meet at $\cos\Theta = \pm\beta_B$.

III. MASSLESS VISIBLE PARTICLE CASES: SMUON PAIR PRODUCTION

For the massless observable particles a_1 and a_2, we now present the general feature based on the previous discussions and demonstrate the observable aspects for the missing mass measurements at the ILC. Throughout this paper, we choose to show the results for the c. m. energy

$$\sqrt{s} = 500\,\mathrm{GeV}.$$

A. The kinematics of cusps and endpoints

A lepton collider is an ideal place to probe the charged slepton sector of the MSSM. To illustrate the basic features of cusps and endpoints at the ILC, we consider smuon pair production. In principle, the scalar nature of the smuon can be determined by the shape of the total cross section near threshold and the angular distributions of the final muons [25]. There are two kinds of smuons, $\tilde{\mu}_L$ and $\tilde{\mu}_R$, scalar partners of the left-handed and right-handed muons respectively. A negligibly small mass of the muon suppresses the left-right mixing and thus makes $\tilde{\mu}_L$ and $\tilde{\mu}_R$ the mass-eigenstates. The smuon pair production in e^+e^- collisions is via s-channel diagrams mediated by a photon or a Z boson. Since the exchanged particles are vector bosons, the helicities of e^+ and e^- are opposite to each other, and only two kinds of pairs, $\tilde{\mu}_R^+\tilde{\mu}_R^-$ and $\tilde{\mu}_L^+\tilde{\mu}_L^-$, are produced. If the lightest neutralino $\tilde{\chi}_1^0$ has a dominant Bino component, $\tilde{\mu}_R$ predominantly decays into $\mu\tilde{\chi}_1^0$. The decay of $\tilde{\mu}_L \to \mu\tilde{\chi}_1^0$ is also sizable. At the ILC, the process $e^+e^- \to \tilde{\mu}_R\tilde{\mu}_R/\tilde{\mu}_L\tilde{\mu}_L \to \mu\tilde{\chi}_1^0 + \mu\tilde{\chi}_1^0$ has a substantial rate. The final state we observe is

$$e^+e^- \to \mu^+\mu^- + \not{E}. \tag{15}$$

This is one good example of the antler process. However, we note that the leading SM process, W^+W^- production followed by $W \to \mu\nu_\mu$, is also of the antler structure.

For illustrative purposes of the signals, we consider two benchmark points for the MSSM parameters, called `Case-A` and `Case-B`, as listed in Table II. These two cases have the same mass spectra, except for the $\tilde{\mu}_L$ mass. In `Case-A`, $\tilde{\mu}_L$ is too heavy for the pair production at $\sqrt{s} = 500\,\mathrm{GeV}$. We have a simple situation where the new physics signal for the final state in Eq. (15) involves only $\tilde{\mu}_R\tilde{\mu}_R$ production. In `Case-B`, the $\tilde{\mu}_L$ mass comes down close to the $\tilde{\mu}_R$ mass, with a mass gap of about 10 GeV. In this case with $m_{\tilde{\mu}_R} \simeq m_{\tilde{\mu}_L}$, the cross

Label	$\tilde{\mu}_R$	$\tilde{\mu}_L$	$\tilde{\chi}_1^0$	$\tilde{\chi}_2^0$	$\tilde{\chi}_3^0$	$\tilde{\chi}_4^0$	$\tilde{\chi}_1^\pm$	$\tilde{\chi}_2^\pm$
`Case-A` (`Case-B`)	158	636 (170)	141	529	654	679	529	679
`Case-C`	–	–	139	235	504	529	235	515

TABLE II: Illustrative SUSY mass spectrum for `Case-A`, `Case-B` (as introduced in Sec. III A) and `Case-C` (as introduced in Sec. IV). All of the masses are in units of GeV.

section of $\tilde{\mu}_R\tilde{\mu}_R$ production is compatible with that of $\tilde{\mu}_L\tilde{\mu}_L$ production. This is because the left-chiral and right-chiral couplings of the smuon to the Z boson, say $g^L_{\tilde{\mu}\tilde{\mu}Z}$ and $g^R_{\tilde{\mu}\tilde{\mu}Z}$ respectively, are accidentally similar in size:

$$g^L_{\tilde{\mu}\tilde{\mu}Z} = \frac{-1+2\sin^2\theta_W}{2\sin\theta_W\cos\theta_W} \approx -0.64, \quad g^R_{\tilde{\mu}\tilde{\mu}Z} = \frac{\sin\theta_W}{\cos\theta_W} \approx 0.55. \tag{16}$$

In `Case-B`, three signals from $\tilde{\mu}_R\tilde{\mu}_R$, $\tilde{\mu}_L\tilde{\mu}_L$, and W^+W^- all have the same antler decay topology. The goal is to disentangle the information and achieve the mass measurements of $\tilde{\mu}_R$, $\tilde{\mu}_L$, and $\tilde{\chi}_1^0$.

It is noted that the LHC searches for slepton direct production does not reach enough sensitivity with the current data yet [26] and would be very challenging in Run-II as well for the parameter choices under consideration, due to the small signal cross section, large SM backgrounds, and the disfavored kinematics of the small mass difference. On the other hand, once crossing the kinematical threshold at a lepton collider, the slepton signal could be readily established.

In Table III, we list the values of various kinematic cusps and endpoints for the five variables discussed above. The mass spectra of the $\tilde{\mu}_R\tilde{\mu}_R$ antler and the W^+W^- antler apply to both `Case-A` and `Case-B`, while that of $\tilde{\mu}_L\tilde{\mu}_L$ applies only to `Case-B`. With the given masses, all of the minimum, cusp, and maximum positions are determined. They are considerably different from each other, indicating important complementarity of these kinematic variables.

In Fig. 2, we show the normalized distributions of (a) $m_{\mu\mu}$, (b) $m_{\rm rec}$, (c) $\cos\Theta$, (d) E_μ, and (e) $E_{\mu^+} + E_{\mu^-}$ for $\tilde{\mu}_R\tilde{\mu}_R$, $\tilde{\mu}_L\tilde{\mu}_L$, and W^+W^- production at the ILC with a c.m. energy of 500 GeV. To appreciate the striking features of the distributions, we have only considered the kinematics here. The full results including spin correlations, initial state radiation (ISR), beamstrahlung, and detector smearing effects will be shown, beginning in section 3.3. First, the m_{aa} distributions for $\tilde{\mu}_R\tilde{\mu}_R$, $\tilde{\mu}_L\tilde{\mu}_L$, and W^+W^- production do not show a clear cusp.

$\sqrt{s}$	500 GeV		
Production channel	$\tilde{\mu}_R\tilde{\mu}_R$	$\tilde{\mu}_L\tilde{\mu}_L$	W^+W^-
input (m_B, m_X)	$(158, 141)$	$(170, 141)$	$(m_W, 0)$
$\lvert\cos\Theta\rvert_{\max}$	0.77	0.73	0.95
$(m_{\mu\mu}^{\min}, m_{\mu\mu}^{\text{cusp}}, m_{\mu\mu}^{\max})$	$(0, 12, 91)$	$(0, 21, 137)$	$(0, 13, 487)$
$(m_{\text{rec}}^{\min}, m_{\text{rec}}^{\text{cusp}}, m_{\text{rec}}^{\max})$	$(408, 445, 488)$	$(363, 413, 479)$	$(0, 13, 487)$
$(E_\mu^{\min}, E_\mu^{\max})$	$(6, 46)$	$(11, 69)$	$(7, 243)$
$(E_{\mu\mu}^{\min}, E_{\mu\mu}^{\text{cusp}}, E_{\mu\mu}^{\max})$	$(12, 52, 92)$	$(21, 79, 137)$	$(13, 250, 487)$

TABLE III: The values of various kinematic cusps and endpoints as seen in Fig. 2, for the mass parameters in Table II. All of the masses and energies are in units of GeV.

This is because the c.m. energy is too high compared with the intermediate mass to reveal the m_{aa} cusp, which would become pronounced when $m_B > 0.44\sqrt{s}$ [15]. For $B = \tilde{\mu}_R$, a sharp m_{aa} cusp requires $\sqrt{s} \lesssim 360\,\text{GeV}$. On the contrary, the m_{rec} distributions for $\tilde{\mu}_R\tilde{\mu}_R$ and $\tilde{\mu}_L\tilde{\mu}_L$ in Fig. 2(b) are of the shape of a sharp triangle. This is attributed to the massive X. For W^+W^- production, the missing particles are massless neutrinos, therefore, the m_{aa} distribution is the same as the m_{rec} distribution.

The $\cos\Theta$ distributions of $\tilde{\mu}_R\tilde{\mu}_R$, $\tilde{\mu}_L\tilde{\mu}_L$, and W^+W^- in Fig. 2(c) present the same functional behavior, proportional to $1/\sin^3\Theta$. There are two sharp points where the cusp and the maximum merge, which correspond to $\pm|\cos\Theta|_{\max}$. The $\tilde{\mu}_R\tilde{\mu}_R$ and $\tilde{\mu}_L\tilde{\mu}_L$ processes have similar values of $|\cos\Theta|_{\max}$, while the W^+W^- process peaks at a considerably larger value. Figure 2(d) shows the energy distribution of one visible particle μ. The distributions for the smuon signals are flat due to their scalar nature, while the flat distribution for the W^+W^- channel is artificial due to the neglect of spin correlation. We will include the full spin effects from section III C and on.

In principle, the two measurements of $E_\mu^{\min}$ and $E_\mu^{\max}$ can determine the two unknown masses m_B and m_X. However the minimum of E_a can be below the detection threshold as in the $\tilde{\mu}_R$ case of $E_\mu^{\min} \simeq 5.8\,\text{GeV}$. One may thus need another independent observable to determine all the masses. In addition, over-constraints on the involved masses are very useful in establishing the new physics model.

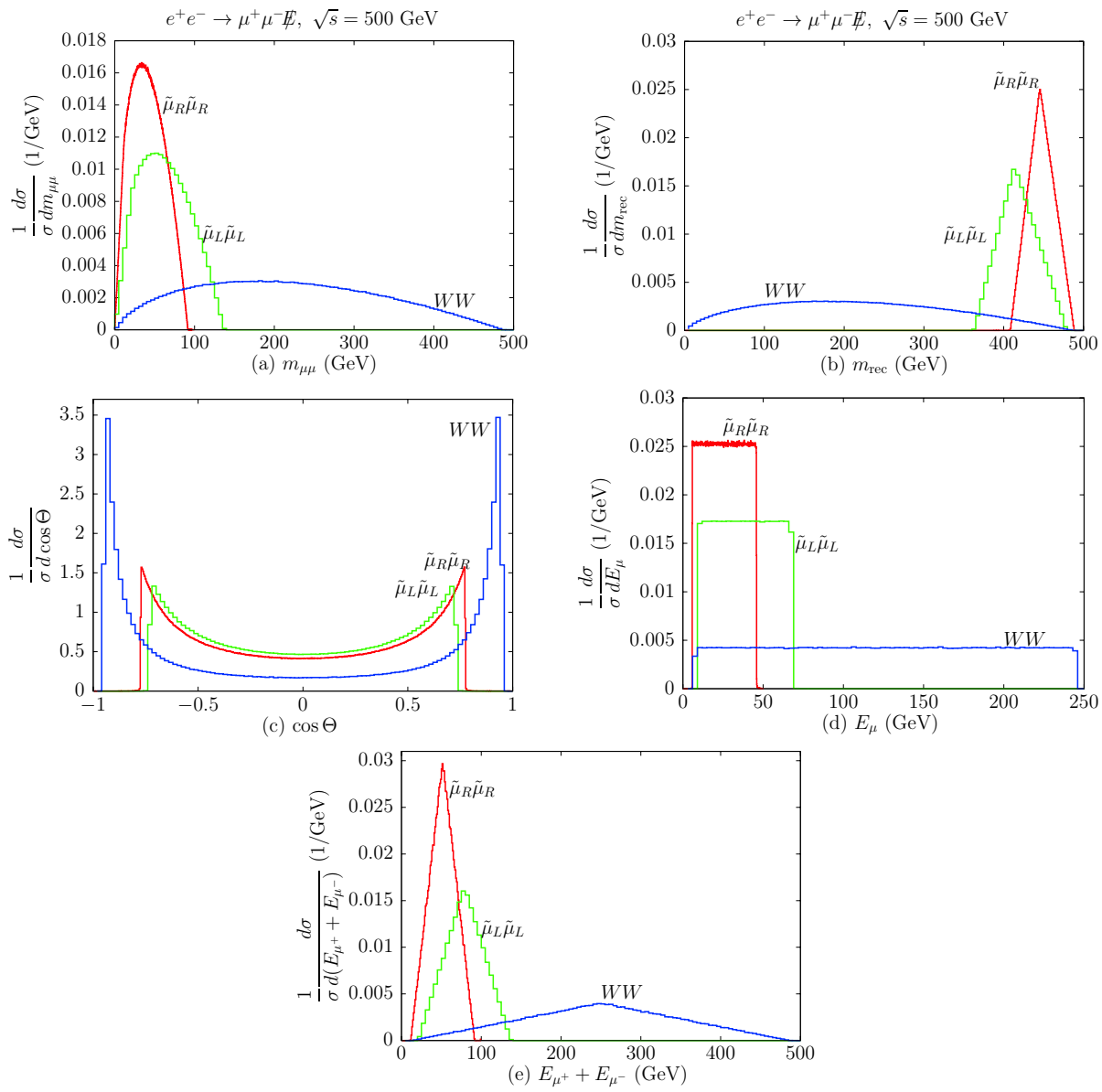

FIG. 2: The normalized distributions of (a) $m_{\mu\mu}$, (b) $m_{\rm rec}$, (c) $\cos\Theta$, (d) E_μ and (e) $E_{\mu^+}+E_{\mu^-}$ for the three cases in Table III, *i.e.*, for $\tilde{\mu}_R\tilde{\mu}_R$, $\tilde{\mu}_L\tilde{\mu}_L$ and W^+W^- production at $\sqrt{s} = 500\,\text{GeV}$. Here we consider only the kinematics without spin correlations.

The distribution of $E_{\mu\mu}(\equiv E_{\mu^+}+E_{\mu^-})$ in Fig. 2(e) is different from the individual energy distribution: the former is triangular while the latter is rectangular. For $\tilde{\mu}_R\tilde{\mu}_R$ and $\tilde{\mu}_L\tilde{\mu}_L$, the E_{aa} distributions are localized so that the pronounced cusp is easy to identify. For W^+W^-, however, the E_{aa} distribution is widespread.

In order to further understand the singular structure, we examine four representative configurations in terms of $(\cos\theta_1, \cos\theta_2)$, where θ_1 and θ_2 are the polar angle of a_1 and a_2

in the rest frame of their parent particles B_1 and B_2, respectively. The correspondence of each corner to a singular point is as follows:

1D configuration						m_{aa}	$m_{\rm rec}$	E_{aa}	E_{XX}
(i)	$\overset{a_2}{\Longleftarrow}$	$\overset{B_2}{\longleftarrow}$	$\overset{e^+e^-}{\bullet}$	$\overset{B_1}{\longrightarrow}$	$\overset{a_1}{\Longrightarrow}$	max	min	max	min
(ii)	$\overset{a_2}{\Longrightarrow}$	$\overset{B_2}{\longleftarrow}$	$\overset{e^+e^-}{\bullet}$	$\overset{B_1}{\longrightarrow}$	$\overset{a_1}{\Longleftarrow}$	cusp	max	min	max
(iii)	$\overset{a_2}{\Longrightarrow}$	$\overset{B_2}{\longleftarrow}$	$\overset{e^+e^-}{\bullet}$	$\overset{B_1}{\longrightarrow}$	$\overset{a_1}{\Longrightarrow}$	min	cusp	cusp	cusp
(iv)	$\overset{a_2}{\Longleftarrow}$	$\overset{B_2}{\longleftarrow}$	$\overset{e^+e^-}{\bullet}$	$\overset{B_1}{\longrightarrow}$	$\overset{a_1}{\Longleftarrow}$	min	cusp	cusp	cusp

(17)

B. The effects of acceptance cuts

In a realistic experimental setting, the previously discussed kinematical features may be smeared, rendering the cusps and endpoints less effective for extracting the mass parameters. We now study the effects of the acceptance cuts.

We first explore the effects due to a missing transverse momentum ($\not{p}_T$) cut, which is essential to suppress the dominant SM background of $e^+e^- \to e^+e^-\mu^+\mu^-$ with the outgoing e^+e^- going down the beam line and not detected. Obviously, the $\not{p}_T$ cut removes some events, reducing the event rate. In addition, the $\not{p}_T$ cut does not apply evenly over the distribution. The positions of the cusp and endpoints can be shifted in some cases.

In Fig. 3, we show the effects of a $\not{p}_T$ cut on the distributions of $m_{\mu\mu}$, $m_{\rm rec}$, $\cos\Theta$, E_μ, and $E_{\mu\mu}$. We normalize each distribution by the total cross section without other kinematic cuts. First, the $m_{\mu\mu}$ distributions with various $\not{p}_T$ cuts are shown in Fig. 3(a) for $\sqrt{s} = 500\,\text{GeV}$ and in Fig. 3(f) for $\sqrt{s} = 350\,\text{GeV}$. The $m_{\mu\mu}$ cusp in the higher c.m. energy case does not present a notable feature while the lower energy case with $\sqrt{s} = 350\,\text{GeV}$ has a more pronounced cusp shape. With a $\not{p}_T > 10\,\text{GeV}$ cut, the m_{aa} distribution retains its triangular shape, but starts to lose the true cusp and maximum positions. The shift is a few GeV. If $\not{p}_T > 20\,\text{GeV}$, the sharp cusp is smeared out and the $m_{\mu\mu}^{\rm max}$ position is shifted by about 10 GeV. In both cases, the $m_{\mu\mu}^{\rm min}$ remains intact. The $m_{\rm rec}$ distribution in Fig. 3(b), on the contrary, keeps its triangular shape even with a high $\not{p}_T$ cut. It is interesting to note that the $\not{p}_T$ cut shifts the $m_{\rm rec}^{\rm min}$ and $m_{\rm rec}^{\rm max}$ while keeping the $m_{\rm rec}^{\rm cusp}$ position fixed. Figure 3(e) presents the distribution of the summed energy of the two visible particles, which are still triangular after the $\not{p}_T$ cut. The cusp position is retained, but the minimum and maximum

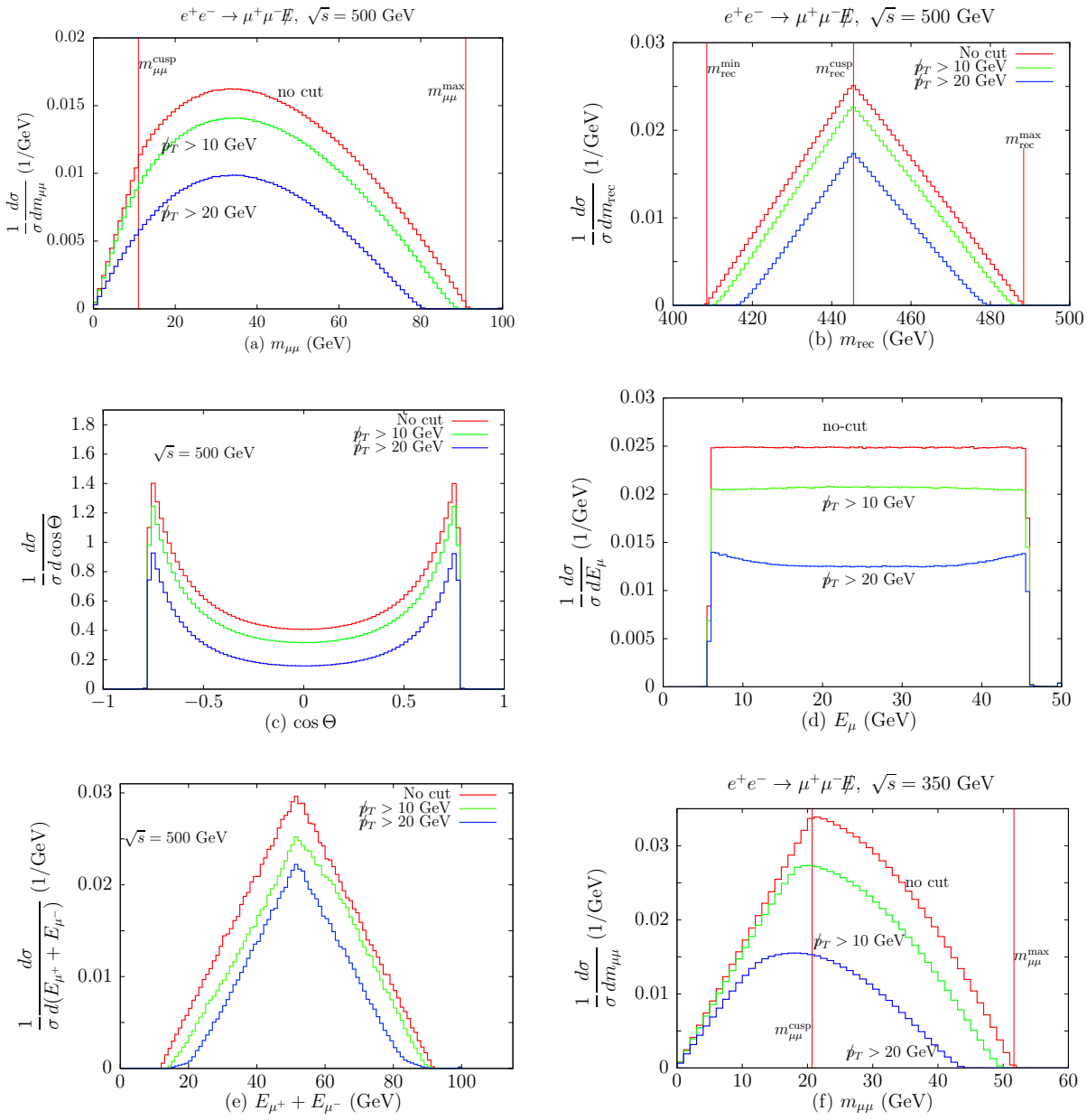

FIG. 3: `Case-A` for $e^+e^- \to \tilde{\mu}_R\tilde{\mu}_R \to \mu^+\mu^- + \not{E}$. Effects due to various $\not{p}_T$ cuts on (a) $m_{\mu\mu}$, (b) $m_{\rm rec}$, (c) $\cos\Theta$, (d) E_μ, and (e) $E_{\mu^+} + E_{\mu^-}$ distributions without spin-correlation and other realistic effects at $\sqrt{s} = 500\,\text{GeV}$. Each distribution is normalized by the total cross section. Panel (f) for the $m_{\mu\mu}$ distribution is set to 350 GeV for comparison.

positions are shifted.

We note that $\not{p}_T$ cut does not affect the positions of the variables $m_{\mu\mu}^{\rm min}$, $m_{\rm rec}^{\rm cusp}$, and $E_{\mu\mu}^{\rm cusp}$ appreciably, which all correspond to the kinematical configurations (*iii*) and (*iv*) in Eq. (17). Here the two visible particles (a_1a_2) move in the same direction, and two invisible particles

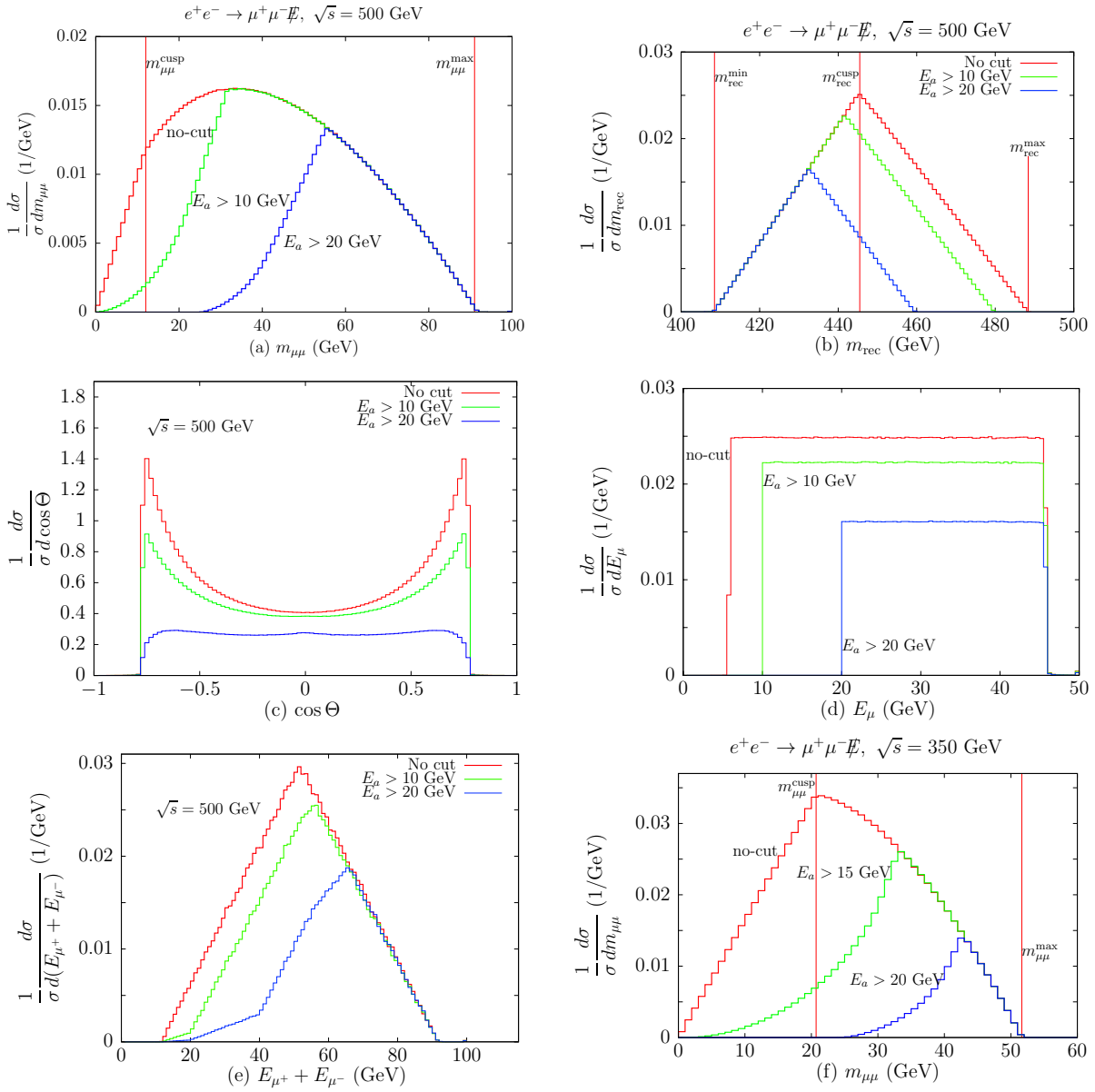

FIG. 4: `Case-A` for $e^+e^- \to \tilde{\mu}_R\tilde{\mu}_R \to \mu^+\mu^-\not{E}$. Effects due to various E_a cuts on the (a) $m_{\mu\mu}$, (b) $m_{\rm rec}$, (c) $\cos\Theta$, (d) E_μ, and (e) $E_{\mu^+} + E_{\mu^-}$ distributions without spin-correlation and other realistic effects at $\sqrt{s} = 500\,\text{GeV}$. Each distribution is normalized by the total cross section without any other acceptance cut. Panel (f) for the $m_{\mu\mu}$ distribution is set to 350 GeV for comparison.

(X_1X_2) move also in the same direction, opposite to the a_1a_2 system. A $\not{p}_T$ cut would not change the system configuration. In contrast, for the configurations (i) and (ii) in Eq. (17), a_1 and a_2 are moving in the opposite direction, and a cut on the X_1X_2 system alters the individual particle as well as the configuration appreciably.

The least affected variable is the $\cos\Theta$ distribution in Fig. 3(c). The $|\cos\Theta|_{\rm max}$ positions remain the same, and the $\not{p}_T$ cut removes the data nearly evenly all over the distribution. Figure 3(d) shows the E_μ distribution under the $\not{p}_T$ cut effects. Similar to the case of $\cos\Theta$, the $\not{p}_T$ cut reduces the whole rate roughly uniformly, and the box-shaped distribution is still maintained.

Figure 4 presents the five kinematic distributions with the effects of the E_a cut. The normalization is done with the total cross section without any cut. Two $m_{\mu\mu}$ distributions are presented, one for $\sqrt{s} = 500\,\text{GeV}$ in Fig. 4(a) and the other for $\sqrt{s} = 350\,\text{GeV}$ in Fig. 4(f). Both retain its maximum position after the E_a cut. However, the $m_{\mu\mu}$ cusp position is shifted by a sizable amount, approximately 10 GeV for $E_a > 15\,\text{GeV}$ cut at $\sqrt{s} = 350\,\text{GeV}$. This behavior is the same for the $E_{\mu\mu}$ distribution in Fig. 4(e). The $m_{\rm rec}$ distribution in Fig. 4(b) behaves oppositely: the maximum and cusp positions are shifted while the minimum position is retained. Therefore, the E_a cut does not change the one-dimensional configuration (i) of Eq. (17).

The $\cos\Theta$ distributions under the E_a cuts are shown in Fig. 4(c). The locations of $|\cos\Theta|_{\rm max}$ remain approximately the same, but the sharp cusps are reduced somewhat. Finally the E_a distribution in Fig. 4(d) shows the expected shift of its minimum into the lower bound on E_a. Note that some data satisfying $E_a > E_a^{\rm cut}$ are also cut off, since the E_a cut has been applied to both of the final leptons. In summary, the acceptance cut distorts the kinematic distributions, and shifts the singular positions. When we extract the mass information from the endpoints, these cut effects must be properly taken into account.

C. Mass measurements with realistic considerations

1. Backgrounds and simulation procedure

For our signal of $e^+e^- \to \mu^+\mu^- + \not{E}$, there are substantial SM backgrounds. The main irreducible SM background is W boson pair production, $e^+e^- \to W^+W^- \to \mu^+\nu_\mu\mu^-\bar{\nu}_\mu$. The next dominant mode is ZZ production, $e^+e^- \to ZZ \to \mu^+\mu^-\nu_i\bar{\nu}_i$ where ν_i denotes a neutrino of all three flavors. The W^+W^- background is larger than the ZZ background by a factor of about 20. In the following numerical simulation, we include the full SM processes for the final state $\mu^+\mu^-\nu\bar{\nu}$.

Another substantial SM background is from $e^+e^- \to e^+e^-\mu^+\mu^-$ where the outgoing e^+ and e^- go down the beam pipe and are missed by the detectors. It is mainly generated by Bhabha scattering with the incoming electron and positron through a t-channel diagram. This background could be a few orders of magnitude larger than the signal. However, a cut on the missing transverse momentum can effectively remove it. The maximum missing transverse momentum in this background comes from the final electron and positron, each of which retains the full energy ($\sqrt{s}/2$ each) and moves within an angle of 1° with respect to the beam pipe (at the edge of the end-cap detector coverage). As a result, most of these background events lie within

$$(\not{p}_T)_{\text{beam line } e^+e^-} \lesssim 3 \times 250\,\text{GeV} \times \sin(1^\circ) \simeq 15\,\text{GeV}. \tag{18}$$

We thus design our basic acceptance cuts for the event selection

$$\begin{aligned} \texttt{Basic cuts:} \qquad & E_a \geq 10\,\text{GeV}, \quad \not{p}_T \geq 15\,\text{GeV}, \\ & |\cos\theta_\ell^{\text{cm}}| \leq 0.9962, \quad m_{aa} \geq 1\,\text{GeV}, \quad m_{\text{rec}} \geq 1\,\text{GeV}. \end{aligned} \tag{19}$$

The angular cut on θ_ℓ^{cm} requires that the observed lepton lies within 5° from the beam pipe. This angular acceptance and the invariant mass cut on the lepton pair regularize the perturbative singularities. We also find that the $\not{p}_T$ cut removes the background from $e^+e^- \to e^+e^-\tau^+\tau^-$ [29].

In principal, the full SUSY backgrounds should be included in addition to the $\tilde{\mu}_R$ and $\tilde{\mu}_L$ signal pair production. There are many types of SUSY backgrounds. The dominant ones are the production of $\tilde{\chi}_1^0\tilde{\chi}_{j\geq 2}^0$ followed by the heavier neutralino decay of $\tilde{\chi}_{j\geq 2}^0 \to \ell^+\ell^-\tilde{\chi}_1^0$. However, their contributions are negligible with our mass point and event selection.

At the ILC environment, it is crucial to consider the other realistic factors in order to reliably estimate the accuracy for the mass determination. These include the effects of ISR, beamstrahlung [30] and detector resolutions. For these purposes, we adopt the ILC-Whizard setup [31], which accommodates the SGV-3.0 fast detector simulation suitable for the ILC [36].

2. *Case-A: $\tilde{\mu}_R\tilde{\mu}_R$ pair production*

For the mass spectrum in Case-A, Fig. 5 presents a full simulation of the five kinematic distributions at $\sqrt{s} = 500\,\text{GeV}$ with the basic cuts in Eq. (19). The solid (red) line denotes

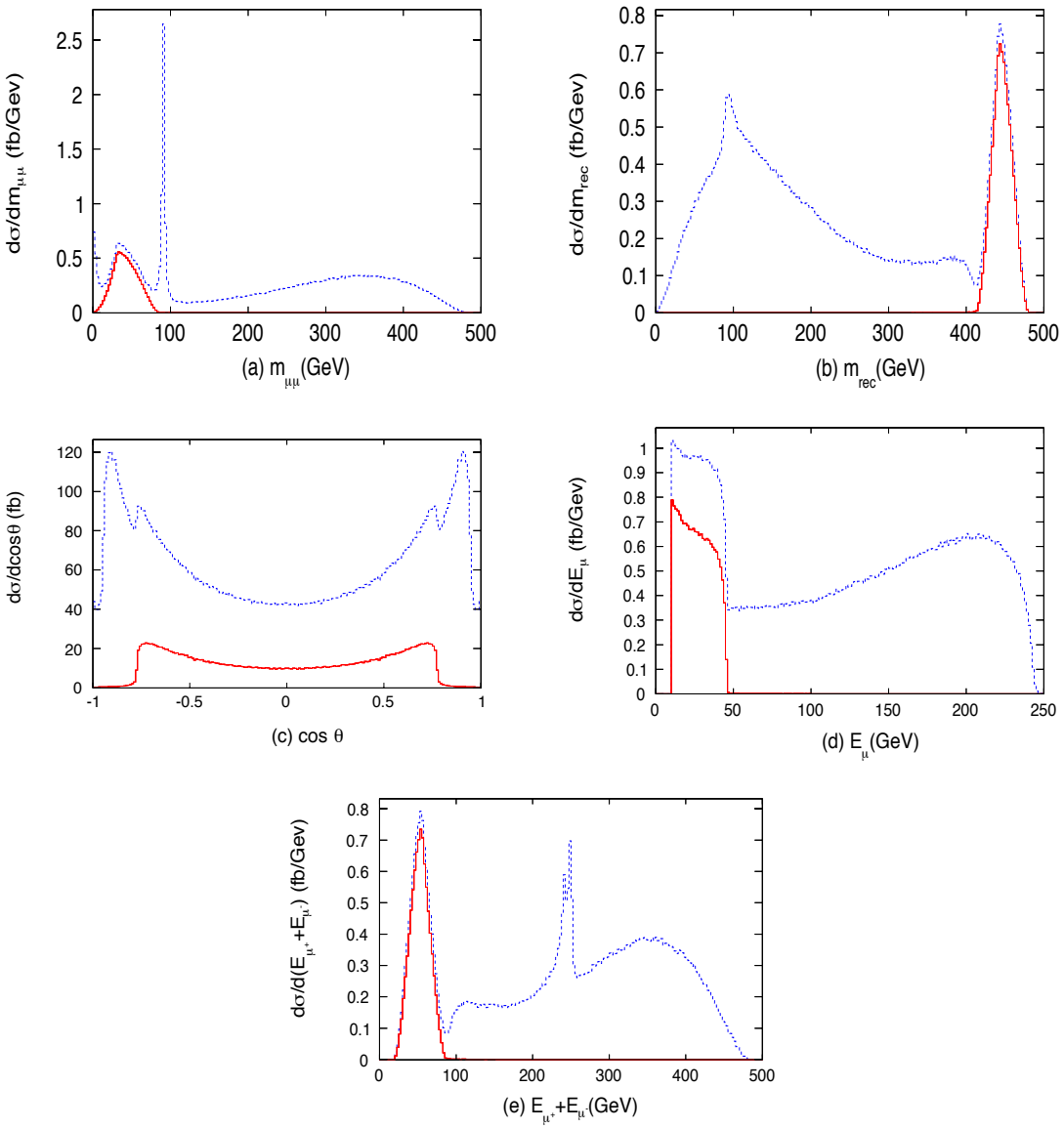

FIG. 5: `Case-A` for $e^+e^- \to \tilde{\mu}_R\tilde{\mu}_R \to \mu^+\mu^-\not{E}$. Basic acceptance cut on the (a) $m_{\mu\mu}$, (b) $m_{\rm rec}$, (c) $\cos\Theta$, (d) E_μ, and (e) $E_{\mu^+} + E_{\mu^-}$ distributions with spin-correlation and other realistic effects. The c.m. energy is set to $\sqrt{s} = 500\,\text{GeV}$ for all distributions. The solid (red) line denotes our signal of the resonant production of a $\tilde{\mu}_R$ pair. The dashed (blue) line is the total event including our signal and the SM backgrounds.

our signal of the resonant production of a $\tilde{\mu}_R\tilde{\mu}_R$ pair. The dashed (blue) line is the total distribution including our signal and the SM backgrounds.

The $m_{\mu\mu}$ distribution from our signal in Fig. 5(a) does not reveal the best feature of the antler process. Its cusp is not very pronounced and its maximum is submerged under the

dominant Z pole. As discussed before, this is because the c.m. energy of 500 GeV is too high compared with the smuon mass. On the contrary, the $m_{\rm rec}$ distribution in Fig. 5(b) separates our signal from the SM backgrounds well. A sharp triangular shape is clearly seen above the SM background tail. This separation is attributed to the weak scale mass of the missing particle X. If X were much lighter such as $M_X \simeq 10\,\text{GeV}$, the cusp position in the $m_{\rm rec}$ distribution of the signal would be shifted to a lower value and thus overlap with that of the large W^+W^- background.

Figure 5(c) presents the $\cos\Theta$ distributions with the W^+W^- background and the $\tilde{\mu}_R\tilde{\mu}_R$ signal. However, the highest point of $\cos\Theta$ (the cusp location) is shifted from the location of the $|\cos\Theta|_{\rm max}$ in Table III, by about $2 \sim 3\%$. This is from the kinematical smearing due to ISR and beamstruhlung effects.

Figure 5(d) shows the muon energy distribution, which consists of two previously box-shaped distributions. Our signal distribution, which is expected to be flat for a scalar boson, is distorted by ISR. The SM background, mainly the W^+W^- background, shows a more tilted distribution, which has additional effects from spin correlation. The reason for the tilted distribution toward higher E_μ is that the W^+W^- production has the largest contribution from the production of $W_L^-W_R^+$ mediated by a t-channel neutrino [33]. Here W_L^- (W_R^+) denotes the left-handed (right-handed) negatively (positively) charged W boson. W_L^- has the left-handed coupling of ℓ_L^--$\bar{\nu}_R$-W_L^- so that the decayed ℓ_L^- moves along the parent W^- direction and the $\bar{\nu}$ in the opposite direction. The ℓ^- tends to have higher energy. Even though the E_μ distribution is not flat both for the signal and the backgrounds, their maximum positions are the same as predicted in Table III. However, the minimum position for the W^+W^- distribution is below the acceptance cut while the minimum for the $\tilde{\mu}_R\tilde{\mu}_R$ signal is approximately the same as the cut. The measurement of these minima becomes problematic. As a result, the other kinematic observables discussed here are essential in the measurement of these masses.

Finally Figs. 5(e) presents the energy sum of two visible particles. The distribution for our signal is triangular and separated from the SM backgrounds. Even in the full and realistic simulation, the cusps and endpoints of the signal are very visible. In fact, the signal part of the distribution takes a very similar form to that of $m_{\rm rec}$.

Understanding those kinematic distributions of our signal is of great use to suppress the

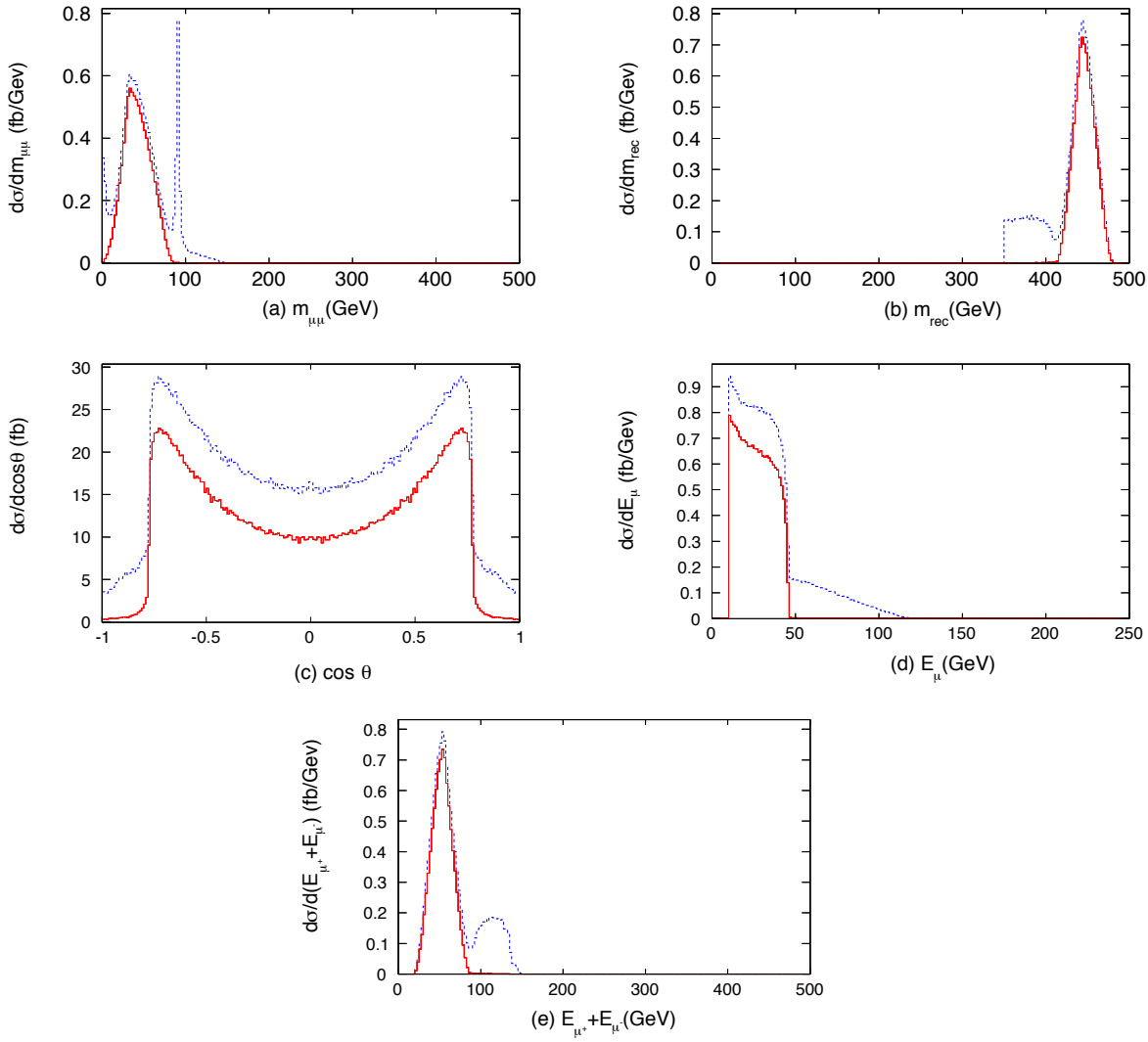

FIG. 6: `Case-A` for $e^+e^- \to \tilde{\mu}_R\tilde{\mu}_R \to \mu^+\mu^-\not{E}$. The effect of an additional cut of $m_{\rm rec} > 350\,{\rm GeV}$ on the (a) $m_{\mu\mu}$, (b) $m_{\rm rec}$, (c) $\cos\Theta$, (d) E_μ, and (e) $E_{\mu^+} + E_{\mu^-}$ distributions with spin-correlation and other realistic effects. The c.m. energy is set to $\sqrt{s} = 500\,{\rm GeV}$ for all distributions. The solid (red) line denotes our signal of the resonant production of a $\tilde{\mu}_R$ pair. The dashed (blue) line is the total differential cross section including our signal and the SM backgrounds.

SM background. For example, we apply an additional cut of

$$m_{\rm rec} > 350\,{\rm GeV}, \tag{20}$$

and present the distributions of the same five kinematic variables in Fig. 6. Our signal, denoted by the solid (red) lines, remains intact since $m_{\rm rec}^{\rm min} = 408\,{\rm GeV}$ for $\tilde{\mu}_R\tilde{\mu}_R$. On the other hand, a large portion of the SM background is excluded. The antler characteristics of

our signal emerge in the total distributions. We can identify all of the cusp structures.

3. `Case-B`: production of $\tilde{\mu}_R\tilde{\mu}_R$ and $\tilde{\mu}_L\tilde{\mu}_L$

We now consider the more complex `Case-B`, where three different antler processes ($\tilde{\mu}_R\tilde{\mu}_R$, $\tilde{\mu}_L\tilde{\mu}_L$, and W^+W^-) are simultaneously involved. In Fig. 7, we present five distributions for `Case-B` at $\sqrt{s} = 500\,\text{GeV}$. Here, the $m_{\rm rec} > 350\,\text{GeV}$ cut has been applied to suppress the main SM backgrounds from W^+W^-. The solid (red) line is the $\tilde{\mu}_R\tilde{\mu}_R$ signal, the dotted (purple) line is from $\tilde{\mu}_L\tilde{\mu}_L$. Finally, the dashed (blue) line is the total differential cross section including our two signals and the SM backgrounds. Note that the total rate for $\tilde{\mu}_R\tilde{\mu}_R$ is compatible with that for $\tilde{\mu}_L\tilde{\mu}_L$.

In Fig. 7(a), we show the $m_{\mu\mu}$ distributions. As expected from the previous analyses, the $\tilde{\mu}_R\tilde{\mu}_R$ signal leads to a cusp structure, while $\tilde{\mu}_L\tilde{\mu}_L$ and W^+W^- do not due to the specific mass and energy relations. On the contrary, the $m_{\rm rec}$ distribution for $\tilde{\mu}_R\tilde{\mu}_R$ denoted by the solid (red) curve and that for $\tilde{\mu}_L\tilde{\mu}_L$ by the dotted (purple) curve do show a triangle: see Fig. 7(b). The SM background is well under-control after the stringent cuts. The challenge is to extract the hidden mass information from the observed overall (dashed blue) curve as a combination of the twin peaks. It is conceivable to achieve this by a fitting procedure based on two triangles. Instead, as done below, we demonstrate another approach by taking advantage of the polarization of the beams.

Figure 7(c) presents the $\cos\Theta$ distribution. The visible $\cos\Theta$ cusp is usually attributed to the lighter intermediate particles ($\tilde{\mu}_R$ in our case). A larger $|\cos\Theta|_{\rm max}$ comes from a smaller m_B with a given c.m. energy. We see that, with our parameter choice, $\tilde{\mu}_R\tilde{\mu}_R$ and $\tilde{\mu}_L\tilde{\mu}_L$ lead to a similar value of $|\cos\Theta|_{\rm max}$, which differ by about 5%.

The E_μ distribution, with the energy endpoint in Fig. 7(d), is known to be one of the most robust variables. Two box-shaped distributions are added to create a two-step stair. Although ISR and beamstrahlung smear the sharp edges, the observation of the two maxima should be quite feasible. On the other hand, the determination of $E_\mu^{\rm min}$ could be more challenging if the acceptance cut for the lepton lower energy threshold overwhelms $E_\mu^{\rm min}$ for $\tilde{\mu}_R\tilde{\mu}_R$, and makes it marginally visible for $\tilde{\mu}_L\tilde{\mu}_L$.

Finally, we present the energy sum distribution of two visible particles in Figs. 7(e). The individual distribution from $\tilde{\mu}_R\tilde{\mu}_R$ and $\tilde{\mu}_L\tilde{\mu}_L$ production leads to impressive sharp triangles,

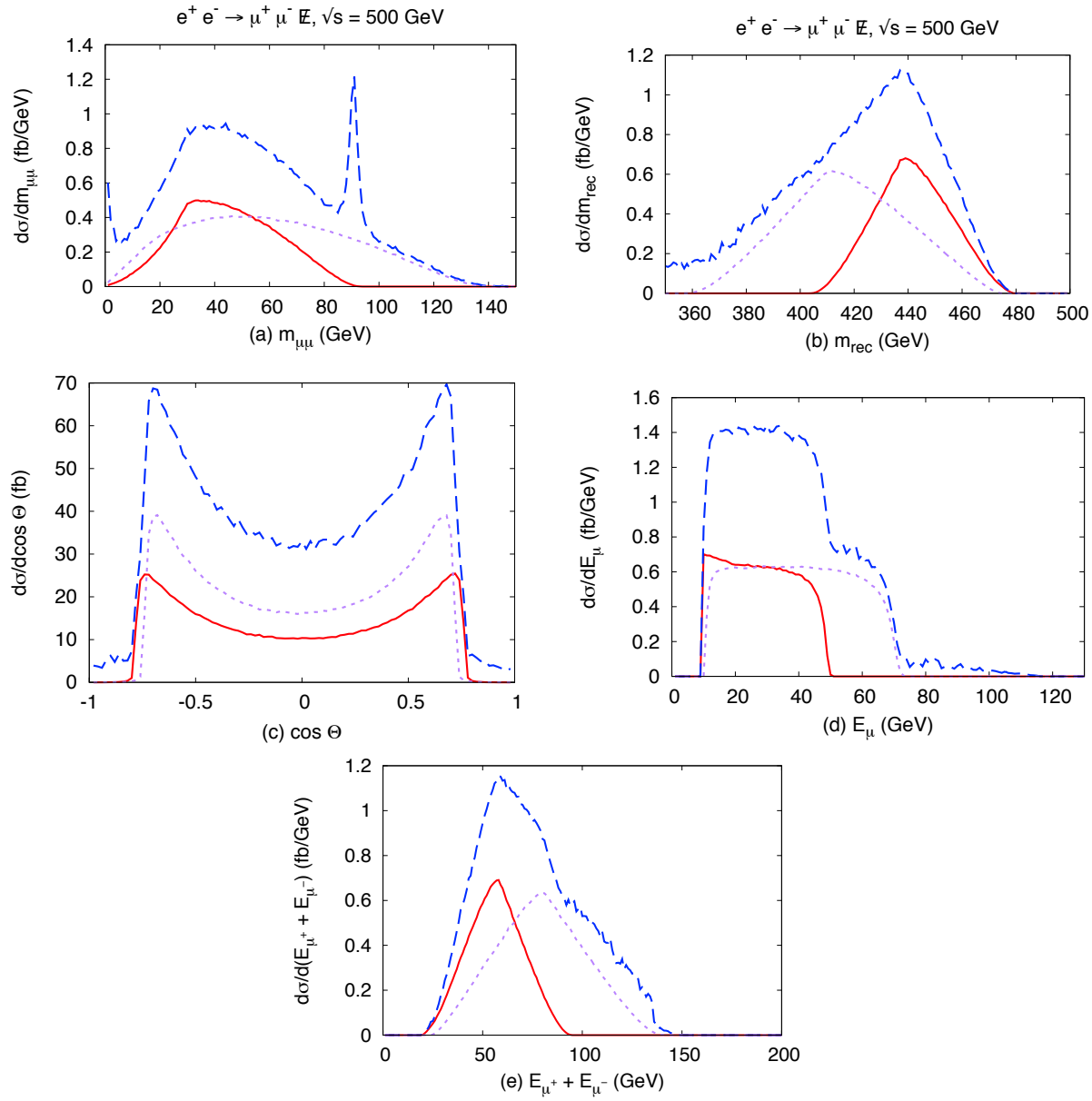
e+ e- → μ+ μ- E, √s = 500 GeV
dσ/dmμμ (fb/GeV)
(a) mμμ (GeV)
e+ e- → μ+ μ- E, √s = 500 GeV
dσ/dmrec (fb/GeV)
(b) mrec (GeV)
dσ/dcos Θ (fb)
(c) cos Θ
dσ/dEμ (fb/GeV)
(d) Eμ (GeV)
dσ/d(Eμ+ + Eμ-) (fb/GeV)
(e) Eμ+ + Eμ- (GeV)

FIG. 7: `Case-B` for $e^+e^- \to \tilde{\mu}_L\tilde{\mu}_L,\ \tilde{\mu}_R\tilde{\mu}_R \to \mu^+\mu^-\not{E}$. The additional cut of $m_{\rm rec} > 350\,\text{GeV}$ is included. We show the (a) $m_{\mu\mu}$, (b) $m_{\rm rec}$, (c) $\cos\Theta$, (d) E_μ, and (e) $E_{\mu^+} + E_{\mu^-}$ distributions with spin-correlation and other realistic effects. The c.m. energy is set $\sqrt{s} = 500\,\text{GeV}$ for all distributions. The solid (red) line corresponds to $\tilde{\mu}_R^+\tilde{\mu}_R^-$, the dotted (purple) line to $\tilde{\mu}_L^+\tilde{\mu}_L^-$. The dashed (blue) line is the total differential cross section including our signal and the SM backgrounds.

as those in Fig. 7(b). The challenge is, once again, to extract the two unknown masses from the observed summed distribution. We next discuss beam polarization as a way to accomplish this.

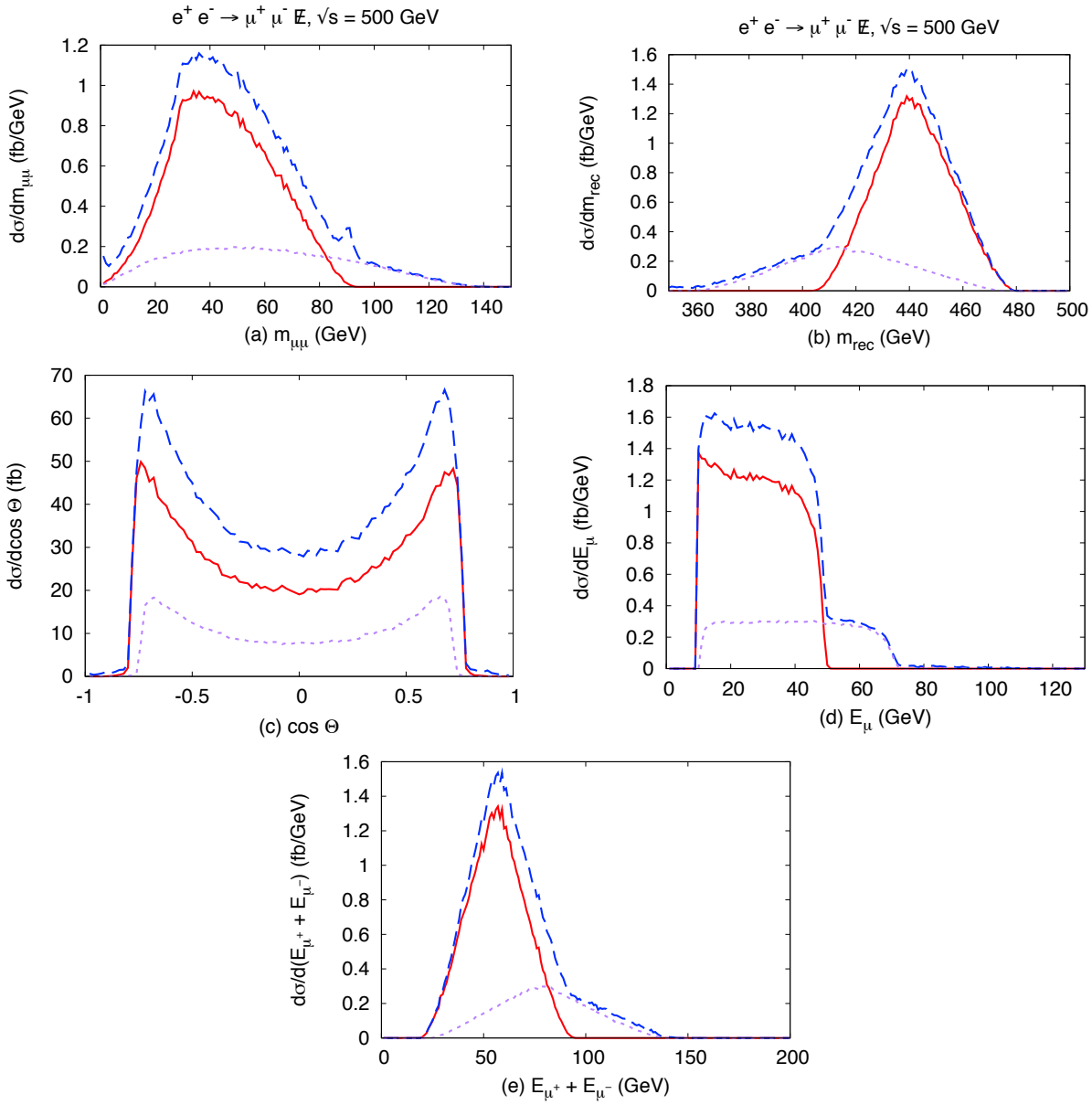
e+ e- → μ+ μ- E, √s = 500 GeV
dσ/dmμμ (fb/GeV)
(a) mμμ (GeV)
e+ e- → μ+ μ- E, √s = 500 GeV
dσ/dmrec (fb/GeV)
(b) mrec (GeV)
dσ/dcos Θ (fb)
(c) cos Θ
dσ/dEμ (fb/GeV)
(d) Eμ (GeV)
dσ/d(Eμ+ + Eμ-) (fb/GeV)
(e) Eμ+ + Eμ- (GeV)

FIG. 8: `Case-B` for $e^+e^- \to \tilde{\mu}_L\tilde{\mu}_L,\ \tilde{\mu}_R\tilde{\mu}_R \to \mu^+\mu^-\not{E}$. Effects of an additional cut of $m_{\rm rec} > 350\,\text{GeV}$ and polarizations $\mathcal{P}_{e^-} = +80\%$ and $\mathcal{P}_{e^+} = -30\%$ on the (a) $m_{\mu\mu}$, (b) $m_{\rm rec}$, (c) $\cos\Theta$, (d) E_μ, and (e) $E_{\mu^+} + E_{\mu^-}$ distributions with spin-correlation and other realistic effects. The c.m. energy is set to $\sqrt{s} = 500\,\text{GeV}$ for all distributions. The solid (red) line corresponds to $\tilde{\mu}_R^+\tilde{\mu}_R^-$, the dotted (purple) line to $\tilde{\mu}_L^+\tilde{\mu}_L^-$. The dashed (blue) line is the total differential cross section including our signal and the SM backgrounds.

All of the distributions show that the two entangled new physics signals as well as the SM backgrounds limit the precise measurements of the cusps and endpoints. The polarization

of the electron and positron beams can play a critical role in disentangling this information. The current baseline design of the ILC anticipates at least 80% (30%) polarization of the electron (positron) beam. By controlling the beam polarization, we can suppress the SM backgrounds and distinguish the two different signals. For the $\tilde{\mu}_R\tilde{\mu}_R$ signal, our optimal setup is $\mathcal{P}_{e^-} = +80\%$ and $\mathcal{P}_{e^+} = -30\%$, denoted by $e^-_R e^+_L$, while for the $\tilde{\mu}_L\tilde{\mu}_L$ signal we apply $\mathcal{P}_{e^-} = -80\%$ and $\mathcal{P}_{e^+} = +30\%$ denoted by $e^-_L e^+_R$.

Figure 8 shows how efficient the right-handed electron beam is at picking out the $\tilde{\mu}_R\tilde{\mu}_R$ signal. For the suppression of the SM backgrounds, we apply the cut of $m_{\rm rec} \geq 350\,{\rm GeV}$. As before, the solid (red) line corresponds to $\tilde{\mu}^+_R\tilde{\mu}^-_R$, the dotted (purple) line to $\tilde{\mu}^+_L\tilde{\mu}^-_L$. The dashed (blue) line is the total differential cross section including our signal and the SM backgrounds. The nearly right-handed electron beam suppresses the SM background as well as the $\tilde{\mu}_L\tilde{\mu}_L$ signal. Only the $\tilde{\mu}_R\tilde{\mu}_R$ signal stands out. The main SM background is through the resonant W^+W^- production. The left-handed coupling of e-ν_e-W is suppressed by the right-handed electron beam. Another interesting feature is that the Z-pole in the $m_{\mu\mu}$ distribution is also very suppressed. A significant contribution to the Z-pole is from $e^+e^- \to \nu_e\bar{\nu}_e Z$ process where Z is via WW fusion. Again the left-handed coupling of the charged current is suppressed by the right-handed electron beam.

The advantage of the cusp is clearly shown here. Its peak structure is not affected. However, the endpoints $m^{\rm min}_{\rm rec}$, $E^{\rm min}_\mu$, and $E^{\rm max}_{\mu\mu}$ do overlap with the backgrounds, although the right-handed polarization removes a large portion of the SM backgrounds. We also observe that $m^{\rm max}_{\rm rec}$, $E^{\rm max}_\mu$, and $E^{\rm min}_{\mu\mu}$ are not contaminated. In summary, the mass measurement of $\tilde{\mu}_R$ and $\tilde{\chi}^0_1$ through the cusps and endpoints is well benefitted by the right-handed polarization of the electron beam.

The left-handed $\tilde{\mu}_L\tilde{\mu}_L$ signal is more difficult to probe since its left-handed coupling is the same as the SM background. In Fig. 9, we set $\mathcal{P}_{e^-} = -80\%$ and $\mathcal{P}_{e^+} = +30\%$ with the additional cut of $m_{\rm rec} > 350\,{\rm GeV}$. From the $m_{\mu\mu}$ distribution, we see that the Z-pole is still strongly visible and the round $m^{\rm cusp}_{\mu\mu}$ for the $\tilde{\mu}_L\tilde{\mu}_L$ signal is very difficult to identify. The total $m_{\rm rec}$ distribution in Fig. 9(b) does not show the sharp triangular shape of the antler decay topology either. The individual triangular shapes of the $\tilde{\mu}_R\tilde{\mu}_R$ and $\tilde{\mu}_L\tilde{\mu}_L$ signals along with the SM background are combined into a rather featureless bump-shaped distribution. Although there is a peak point, it is hard to claim as a cusp. The $\cos\Theta$ distribution in Fig. 9(c) shows one of the most characteristic features of the antler topology. Two sharp

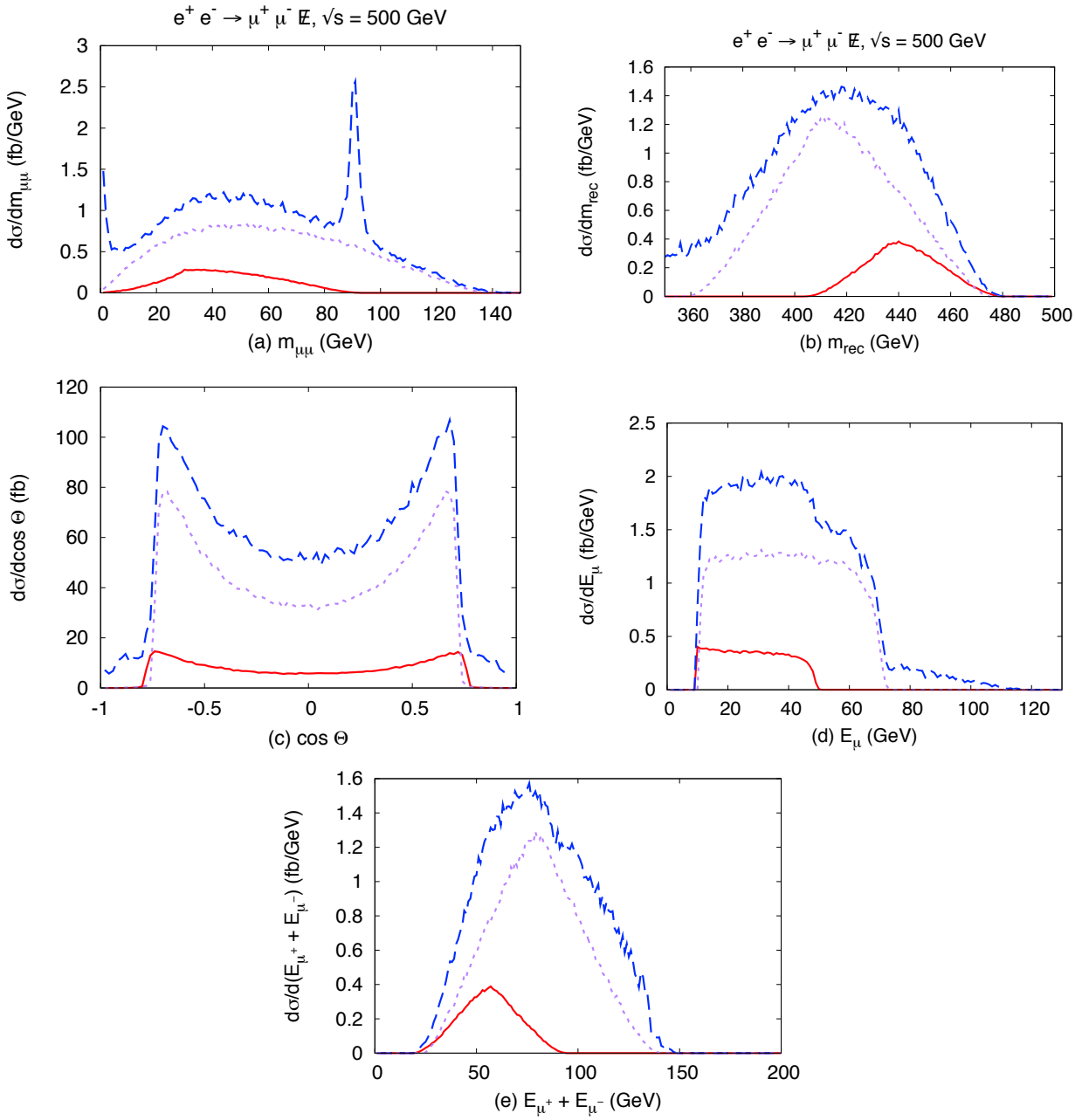
e+ e- → μ+ μ- E, √s = 500 GeV
dσ/dmμμ (fb/GeV)
(a) mμμ (GeV)
e+ e- → μ+ μ- E, √s = 500 GeV
dσ/dmrec (fb/GeV)
(b) mrec (GeV)
dσ/dcos Θ (fb)
(c) cos Θ
dσ/dEμ (fb/GeV)
(d) Eμ (GeV)
dσ/d(Eμ+ + Eμ-) (fb/GeV)
(e) Eμ+ + Eμ- (GeV)

FIG. 9: `Case-B` for $e^+e^- \to \tilde{\mu}_L\tilde{\mu}_L,\ \tilde{\mu}_R\tilde{\mu}_R \to \mu^+\mu^-\not{E}$. Effects of an additional cut of $m_{\rm rec} > 350\,\text{GeV}$ and polarizations $\mathcal{P}_{e^-} = -80\%$ and $\mathcal{P}_{e^+} = +30\%$ on the (a) $m_{\mu\mu}$, (b) $m_{\rm rec}$, (c) $\cos\Theta$, (d) E_μ, and (e) $E_{\mu^+} + E_{\mu^-}$ distributions with spin-correlation and other realistic effects. The c.m. energy is set to $\sqrt{s} = 500\,\text{GeV}$ for all distributions. The solid (red) line corresponds to $\tilde{\mu}_R^+\tilde{\mu}_R^-$, the dotted (purple) line to $\tilde{\mu}_L^+\tilde{\mu}_L^-$. The dashed (blue) line is the total event including our signal and the SM backgrounds.

cusps appear, which correspond to the $\tilde{\mu}_L\tilde{\mu}_L$ signal.

The total E_μ distribution in Fig. 9(d) does not provide quite a clean series of rectangular distributions. The mixture of different contributions from $\tilde{\mu}_R\tilde{\mu}_R$, $\tilde{\mu}_L\tilde{\mu}_L$ and W^+W^- along with the smearing makes reading the maximum points more difficult. The $E_\mu^{\rm min}$ position of the $\tilde{\mu}_L\tilde{\mu}_L$ signal, which is near the kinematic cut, is mixed with the SM backgrounds and the $\tilde{\mu}_R\tilde{\mu}_R$ signal. Finally, the total $E_{\mu\mu}$ distribution loses the triangular shape of the $\tilde{\mu}_L\tilde{\mu}_L$ signal: see Fig. 9(e). Nevertheless the peak position coincides with the cusp position for both energy sum distributions. We can identify them with the cusps.

D. The mass measurement precision

In order to estimate the achievable precision of a measurement of the masses in the presence of realistic effects, we analyze the distributions we have discussed here using the log-likelihood method based on Poisson statistics. A benefit of a log-likelihood analysis is that it compares the full shape of the distribution, not just the position of the cusps and endpoints which, as we have seen, can be smeared and even moved due to realistic collider effects. For our log-likelihood calculation, since we have shown that the background can be almost totally removed by appropriate cuts, we focus on comparing one signal to another with different masses for the smuon and neutralino.

We calculate the log-likelihood as

$$LL(N;\nu) = 2\sum_i \left[N_i \ln\left(\frac{N_i}{\nu_i}\right) + \nu_i - N_i \right] \tag{21}$$

where ν_i is the expected number of events in bin i with the masses set according to `Case-A` and N_i is the number of events expected in bin i for the alternate mass point. For each distribution, we use 50 bins. We take the integrated luminosity to be 100 fb^{-1} and find that the number of signal events is sufficiently large that the probability distribution of the log-likelihood approximates well a χ^2 distribution. We then find that the 95% confidence level value for each log-likelihood is $LL_{95\%} = 67.5$. We scan over the masses of the smuons and neutralinos in steps of 0.25 GeV, calculate the log-likelihood for each mass point, and plot the contour where it is equal to 67.5 in Fig. 10 for four kinematical variables assuming `Case-A`. These are the 95% confidence lines for each kinematical variable considered separately.

Considering the kinematics variables of $m_{\mu\mu}$ (red), m_{rec} (blue), $\cos\Theta$ (green), and E_μ (purple), we present the 95% C.L. allied contours in the parameter space of $(\Delta m_{\tilde{\chi}_1^0}, \Delta m_{\tilde{\mu}_R})$

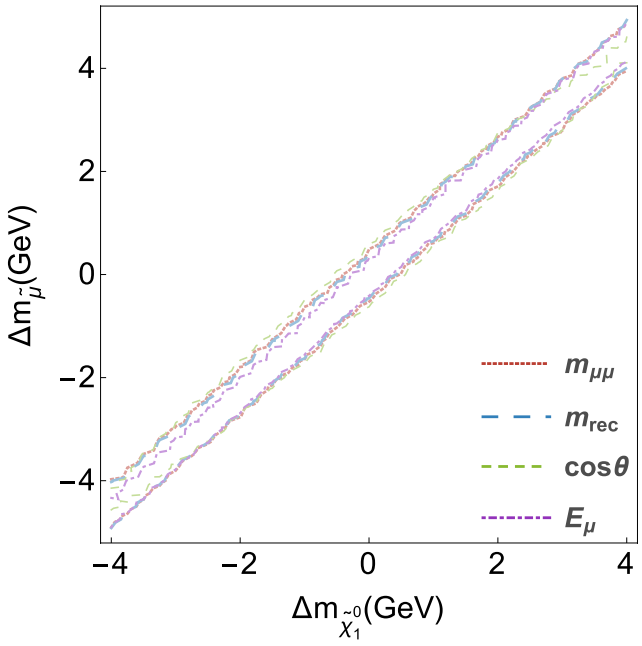

FIG. 10: For `Case-A` for $e^+e^- \to \tilde{\mu}_R\tilde{\mu}_R \to \mu^+\mu^-\not{E}$, the 95% C.L. contours for the precision of the mass measurement in the parameter space of $(\Delta m_{\tilde{\chi}_1^0}, \Delta m_{\tilde{\mu}_R})$. An additional cut of $m_{\rm rec} > 350\,\text{GeV}$ on the distributions with spin-correlation and other realistic effects are included. The c.m. energy is set to $\sqrt{s} = 500\,\text{GeV}$ for all distributions and the integrated luminosity is $100\,\text{fb}^{-1}$.

in Fig. 10. All the variables are roughly equally good at measuring the two masses, leading to an accuracy of approximately $\pm 0.5\,\text{GeV}$ (for clarity of the presentation, we have left out the contours for $E_{\mu\mu}$ and $E_{\rm rec}$).

We also find that our kinematical variables are very sensitive if we vary one mass parameter with the other fixed. However, the determination for the two masses is correlated, as seen from Fig. 10 with a linear band rather than a closed ellipse in the plotted region. This is due to the fact that the cusps and endpoints depend on the masses mainly as a ratio rather than independently, as can be seen in Eqs. (7), (10), and (12). The ellipse shape of the contour will become manifest when extending to larger regions.

We have also considered the effect of combining these measurements in a joint test-statistic including a calculation of the correlation between these variables. The magnitude of the correlation is quantified by the ratio of the off-diagonal term to the diagonal term of the covariance matrix. We found that the correlation among $m_{\rm rec}$, E_μ and $\cos\Theta$ was negligible (the off-diagonal terms of the covariance matrix was a few percent or smaller

compared to the diagonal terms), the correlation between $m_{\rm rec}$ and $E_{\mu\mu}$ was small but non-negligible (the off-diagonal term was approximately 8% of the diagonal terms), and $E_{\mu\mu}$ and $E_{\rm rec}$ were fully correlated as expected (the off-diagonal term was the same size as the diagonal term). However, we did not find appreciable improvement in the precision of the mass measurements by combining the log-likelihoods. This is due partly to the correlation between these variables, partly to the differences in how the log-likelihood depends on each of these variables, and partly to the properties of the χ^2 distribution when test statistics with a large number of degrees of freedom are combined as we briefly explain in Appendix A.

IV. MASSIVE VISIBLE PARTICLE CASE: CHARGINO PAIR PRODUCTION

It is quite likely that the DM particles will be accompanied by other massive observable final states in the decay process. Although the nature of the cusps is similar to the previous discussions, the characteristic features and their observability may be different. An important example of this type of kinematics is in chargino pair production followed by the chargino's decay into a W and a $\tilde{\chi}_1^0$. This process is a typical antler process, which is different from the smuon pair production in that the visible particle W is massive. In order to fully reconstruct the kinematics of the W, we consider the case where the W boson decays hadronically. Our signal event selection is

$$e^+e^- \to \tilde{\chi}_1^+\tilde{\chi}_1^- \to W^+W^-\tilde{\chi}_1^0\tilde{\chi}_1^0 \to jj, jj + \tilde{\chi}_1^0\tilde{\chi}_1^0. \tag{22}$$

For illustrative purposes, we consider the `Case-C` in Table II.

For the LHC searches of gaugino production, there is no sensitivity with the current data yet [27] for the parameter choices under consideration, due to the disfavored kinematics of the small mass difference and the large SM backgrounds. The upcoming Run II at 13 TeV will likely reach the sensitivity to cover this parameter region [28]. It is thus exciting to look forward to the LHC outcome. Should a SUSY signal be observed at the LHC, it would strongly motivate the ILC experiment to further study the SUSY property and to determine the missing particle mass as proposed in this work.

The distributions of the invariant mass of W^+W^- and $\tilde{\chi}_1^0\tilde{\chi}_1^0$ follow the same characteristic function where now the visible particle W is massive. The cusp and endpoint positions of

$\sqrt{s}$	Channel	(m_B, m_X, m_a)	$(m_{WW}^{\rm min}, m_{WW}^{\rm cusp}, m_{WW}^{\rm max})$	$(m_{\rm rec}^{\rm min}, m_{\rm rec}^{\rm cusp}, m_{\rm rec}^{\rm max})$
500	$\tilde{\chi}_1^+\tilde{\chi}_1^-$	$(235, 139, m_W)$	$(161, 171, 221)$	$(279, 296, 338)$
		$(E_W^{\rm min}, E_W^{\rm max})$	$(E_{WW}^{\rm min}, E_{WW}^{\rm cusp}, E_{WW}^{\rm max})$	$(E_{XX}^{\rm min}, E_{XX}^{\rm cusp}, E_{XX}^{\rm max})$
		$(81, 111)$	$(162, 190, 221)$	$(278, 309, 338)$

TABLE IV: The values of various kinematic cusps and endpoints for the mass parameters in the `Case-C`. All the masses and energies are in units of GeV.

these distributions can be obtained from Table I. The $\cos\Theta$ distribution for the massive visible particle case does not present a sharp cusp or endpoint. The E_W distribution has a minimum and a maximum as in the massless visible particle case. The distribution of $E_{WW} = E_{W^+} + E_{W^-}$ also accommodates the maximum, cusp and minimum. In Table IV, we present the values of the cusps and endpoints for `Case-C`.

The reconstruction of the variables m_{WW}, $m_{\rm rec}$, and E_{WW} is straightforward in terms of the jets and the known collision frame. In order to reconstruct E_W and $\cos\Theta$, we split the jets into two pairs and require each pair to reconstruct an invariant mass near m_W. We then note that due to the symmetry of the antler decay topology, the E_{W^+} and E_{W^-} distributions are equal to each other and the $\cos\Theta$ distribution is symmetric with respect to an interchange of W^+ and W^-. As a result, the E_W and $\cos\Theta$ distributions can be obtained by averaging the distributions for each W.

In addition to our basic cuts outlined in Eq. (19), we have applied the following cuts

$$\Delta R_{jj} \equiv \sqrt{(\Delta\eta_{jj})^2 + (\Delta\phi_{jj})^2} \geq 0.4 \ , \qquad (23)$$
$$|m_{jj} - m_W| < 5\Gamma_W \ , \quad m_{\rm rec} > 120\,{\rm GeV} \ ,$$

where the jet separation ΔR_{jj} is between all pairs of jets, m_{jj} is only between pairs of jets identified with the W, and the $m_{\rm rec} > 120\,{\rm GeV}$ cut removes most of the remaining SM background. Again, we adopt the standard simulation packages ILC-Whizard setup [31], including the SGV-3.0 fast detector simulation suitable for the ILC [36].

In Fig. 11, the solid (red) lines denote our chargino signal. The dotted (blue) lines give the total differential cross section including our signal and the SM backgrounds. The SM backgrounds are computed through the full two-to-six processes $e^+e^- \to jjjj\nu\bar{\nu}$ which includes the full spin correlation.

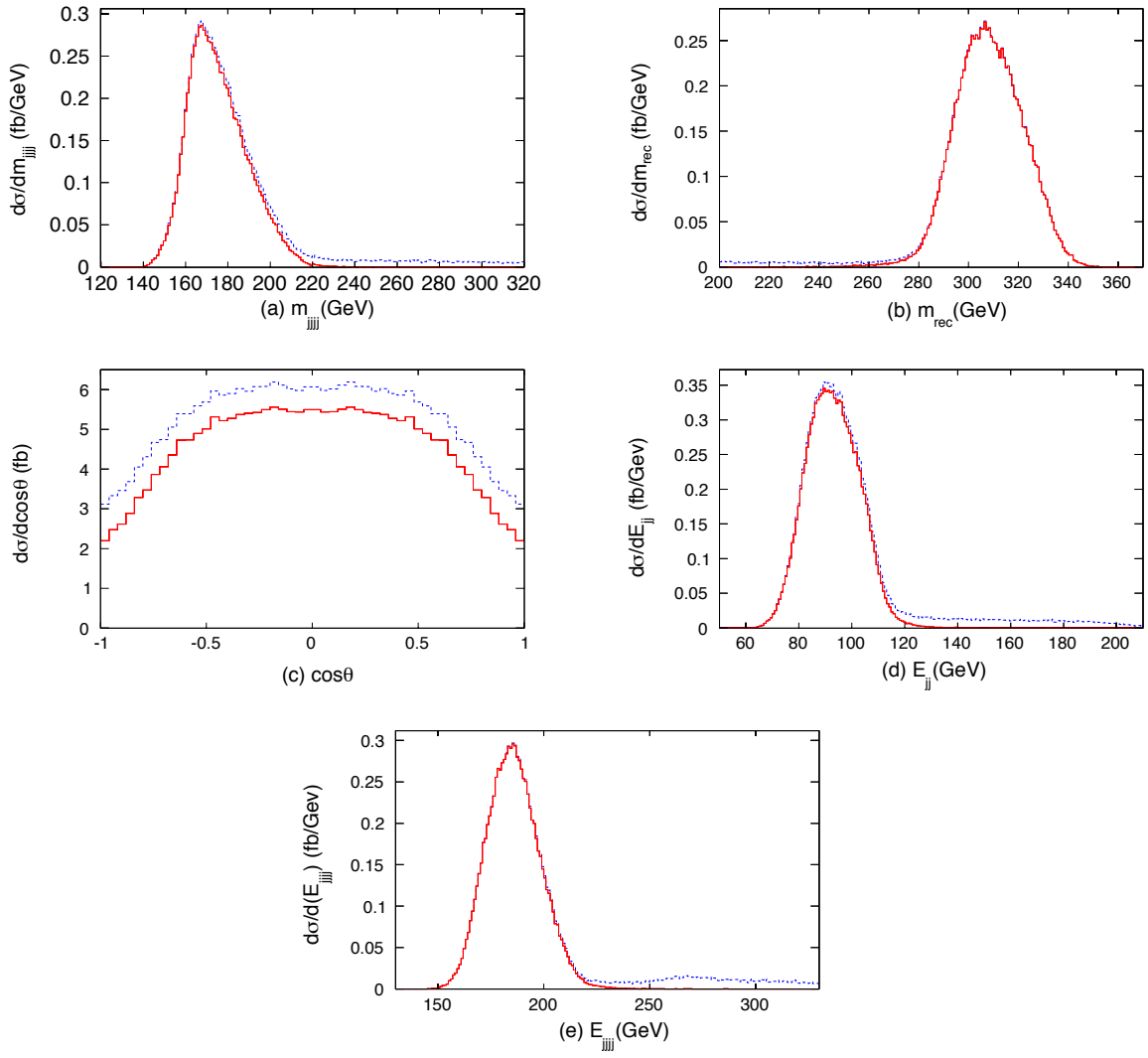

FIG. 11: `Case-C` for $e^+e^- \to jj, jj\not{E}$ with an additional cut of $m_{\rm rec} \geq 120\,{\rm GeV}$ and $|m_{jj} - m_W| < 5\Gamma_W$. We show the (a) m_{jjjj}, (b) $m_{\rm rec}$, (c) $\cos\Theta$, (d) E_{jj}, and (e) E_{jjjj} distributions with spin-correlation and other realistic effects. The c.m. energy is set to $\sqrt{s} = 500\,{\rm GeV}$ for all distributions. The solid (red) line denotes our signal of the resonant production of a chargino pair. The dashed (blue) line is the total differential cross section including our signal and the SM backgrounds.

Figures 11(a) and (b) show the invariant mass distributions of four jets and two invisible particles, respectively. Realistic effects smear the sharp m_{jjjj} and $m_{\rm rec}$ distributions significantly. In particular, the locations of $m_{jjjj}^{\rm min}$ and $m_{\rm rec}^{\rm min}$ are shifted to lower values by about 20 GeV from the expected values with kinematics alone in Table IV. This is mainly due to detector smearing. The $m_{jjjj}^{\rm cusp}$ and $m_{jjjj}^{\rm max}$ are respectively in agreement with the $m_{WW}^{\rm cusp}$ and

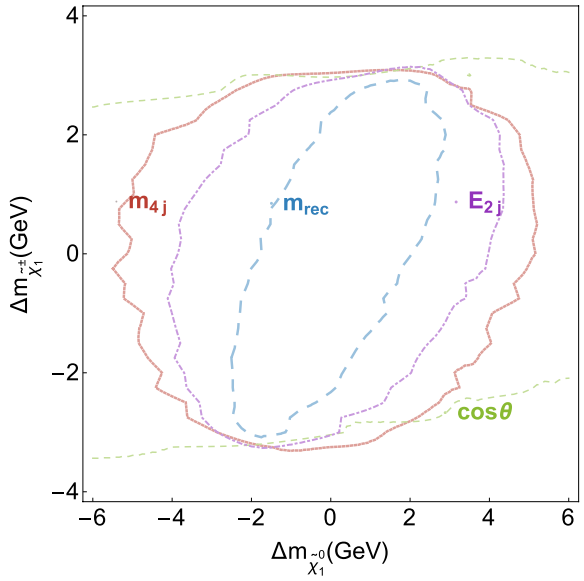

FIG. 12: `Case-C` for $e^+e^- \to jj, jj + \not{E}$, the 95% C.L. contours for the precision of the mass measurement in the parameter space of $(\Delta m_{\tilde{\chi}_1^0}, \Delta m_{\tilde{\chi}_1^\pm})$. The additional cuts of $m_{\rm rec} \geq 120\,{\rm GeV}$ and $|m_{jj} - m_W| < 5\Gamma_W$ are included in the distributions as well as spin-correlation and other realistic effects. The c.m. energy is set to $\sqrt{s} = 500\,{\rm GeV}$ for all distributions and the integrated luminosity is $100\,{\rm fb}^{-1}$.

$m_{WW}^{\rm max}$ values in Table IV but are significantly smeared. The $m_{\rm rec}^{\rm cusp}$ and $m_{\rm rec}^{\rm max}$ are larger by about 10 GeV than the expected values. As commented earlier, the $\cos\Theta$ distribution in Fig. 11(c) does not have a sharp cusp even before including realistic effects.

Figure 11(d) presents the E_{jj} distribution which is significantly smeared and the sharp edges are no longer visible due to jet energy resolution effects. The expected values of $E_W^{\rm min}$ and $E_W^{\rm max}$ cannot be read from this distribution. In Fig. 11(e), we show the distribution of E_{jjjj}. The expected triangular shapes can be seen but the sharp features are smeared due to the realistic considerations. Their minimum and maximum positions are moved to approximately 10 GeV lower and higher values, respectively, while the cusp position identified with the peaks remains near the expected values.

We perform a log-likelihood analysis for the massive visible particle case and present the 95% C.L. contours for the mass measurement of $\tilde{\chi}_1^0$ and $\tilde{\chi}_1^\pm$ in Fig. 12. Remarkable is that $m_{\rm rec}$ leads to the most precise mass measurement, not the commonly considered variable E_W, especially on the missing particle mass. The E_W measurement leads to about

$\Delta m_{\tilde{\chi}_1^0} \simeq \pm 4$ GeV precision while the $m_{\rm rec}$ improves into ± 2 GeV. This is due to the fact that the cusp peak position is more stable with respect to detector smearing effects, compared with the sharp energy endpoint. The intermediate chargino mass precision is about 2 GeV both by E_W and $m_{\rm rec}$. The mass measurement precision is not as good as that of the smuon pair production, because of inferior hadronic four jet measurement here.

To appreciate the improvement for the missing mass measurement with our antler approach, we have compared it with the standard "mono-photon" signal, $e^+e^- \to \gamma \not{E}$ [23, 34]. Although this is the most model-independent method, the measurement of the endpoint in a slowly-varying E_γ spectrum results in rather poor sensitivity. Besides the potential model-dependence of the signal cross section, we find that the background $e^+e^- \to \gamma\nu\bar{\nu}$ is about 100 times larger than the signal for the benchmark point of Ref. [34]. We have performed the log-likelihood analysis and find that the best accuracy for the lightest neutralino mass determination would be no better than about 50 GeV.

V. SUMMARY AND CONCLUSIONS

WIMP dark matter below or near the TeV scale remains a highly motivated option. To convincingly establish a WIMP DM candidate, it is ultimately important to reach consistency between direct searches and collider signals for the common parameters of mass, spin and coupling strength [35].

Through the processes of antler decay topology at a lepton collider, $e^+e^- \to B_1B_2 \to X_1a_1 + X_2a_2$, we studied a new method for measuring the missing particle mass (m_X) and the intermediate particle mass (m_B): the cusp method. With this special and yet common topology, we explored six kinematic experimentally accessible observables, m_{aa}, $m_{\rm rec} \equiv m_{XX}$, $\cos\Theta$, E_a, E_{aa} and $E_{\rm rec} \equiv E_{XX}$. Each of these distributions accommodates singular structures: a minimum, a cusp and a maximum. Their positions are determined by the kinematics only, *i.e.*, the masses of B, a, X and $\sqrt{s}$, providing a powerful method to measure the particle masses m_B and m_X. We presented the analytic expressions for their positions in terms of their masses in section II. We chose to study the accuracy for the mass determination at a lepton collider with three benchmark scenarios in the framework of the MSSM, as listed in Table II, and named `Case-A`, `Case-B`, and `Case-C`.

`Case-A` is the simplest illustration where only a right-handed smuon ($\tilde{\mu}_R$) pair is kine-

matically accessible. `Case-B` is slightly more complicated since both right-handed and left-handed ($\tilde{\mu}_L$) smuon pairs can be produced. We consider the clean leptonic final state of $\mu^+\mu^-\not{E}$ from the smuon decays. By presenting the signal kinematics, we first confirmed the analytic expressions numerically in Fig. 2. We showed that, except for m_{aa}, due to an anticipated kinematical reason, all the other variables yield the pronounced features of a cusp distribution. Although the SM background $e^+e^- \to W^+W^- \to \mu^+\nu_\mu\mu^-\bar{\nu}_\mu$ also results in the antler topology, the positions of the cusps are significantly different due to the massless missing particles, the neutrinos. This difference is used to separate the SM background very efficiently. Furthermore, we pointed out that the experimental acceptance cuts on the observable leptons may change the positions and the shapes of the cusps in a systematic and predictable way, as seen in Figs. 3 and 4.

Through a full simulation including spin correlation, the SM backgrounds, and other realistic effects, we studied how much of the idealistic features of the cusps and endpoints survive, and how well the cusp method determines the missing particle mass for a 500 GeV ILC. We found that the inevitable experimental effects of ISR, beamstrahlung and detector resolutions not only distort the characteristic distributions but also shift the cusp and endpoint positions, as seen in Figs. 5, 6 and 7. The beam polarization may be used to effectively separate the final state $\tilde{\mu}_R\tilde{\mu}_R$ and $\tilde{\mu}_L\tilde{\mu}_L$, as shown in Figs. 8 and 9. To optimize our statistical treatment, we exploited the log-likelihood method based on the Poisson probability function. The precisions for the mass measurement with various variables in `Case-A` were shown in Fig. 10. The accuracy could reach approximately ± 0.5 GeV for smuon pair production, and was comparable for the muon energy endpoint E_μ and the cusp in $m_{\rm rec}$, $E_{\mu\mu}$ or E_{XX}.

In `Case-C`, we studied the chargino pair production with $\tilde{\chi}_1^\pm \to W^\pm\tilde{\chi}_1^0$. We focused on the hadronic decay $W \to jj$ in order to effectively reconstruct the kinematics, and to explore the detector effects on the hadronic final state. The poor energy resolution for the hadronic final state of the W decay smears the cusp and endpoint quite significantly, as shown in Fig. 11. We found that the $m_{\rm rec}$, E_{jjjj} and $E_{\rm rec}$ cusps are more stable than the energy endpoint E_{jj} against realistic experimental effects, and thus provided a more robust mass determination reaching approximately ± 2 GeV. In the previous section, we also made a comparison with the other proposed methods for determining the missing mass at a lepton collider. We see the merits of our approach.

Under the clean experimental environment and well-defined kinematics, a future high energy lepton collider may take advantage of the antler decay topology and provide an accurate determination for the missing particle mass consistent with the WIMP DM candidate.

Acknowledgments

This work is supported in part by the U.S. Department of Energy under grant No. DE-FG02-95ER40896, and in part by PITT PACC. The work of JS is supported by NRF-2013R1A1A2061331.

Appendix A: Log-likelihood combination

We have found that combining the log-likelihoods for our kinematic variables did not significantly improve the achievable accuracy of the mass measurement. The reason for this was a combination of the correlation between the variables, the slight differences in how the log-likelihood depended on each kinematic variable, and how the combination is affected by having a large number of bins in each log-likelihood, as we will now explain.

We have found that the log-likelihood for the variables $m_{\mu\mu}$, $m_{\rm rec}$, E_μ, $E_{\mu\mu}$ and $E_{\rm rec}$ depends approximately quadratically on the mass difference Δm, where Δm is defined to be along the diagonal line with negative slope in Fig. 10,

$$LL = \alpha_{kv} \left(\Delta m\right)^2 \ , \tag{A1}$$

where α_{kv} is a constant to be determined for each kinematic variable. We will consider the optimal situation where the kinematic variables are completely uncorrelated and α_{kv} is the same for each kinematic variable and set $\alpha_{kv} = \alpha$. In this case, the joint test statistic is the sum of the N individual test statistics

$$t_N = N\alpha \left(\Delta m\right)^2 \ . \tag{A2}$$

If the number of bins n is large (which is a good approximation in our case with 50 bins for each log-likelihood), then the individual log-likelihoods and the joint test-statistic are well-approximated by Gaussian distributions with mean $\mu_N = Nn$ and standard deviation $\sigma_N = \sqrt{2Nn}$, where the individual log-likelihoods have $\mu_1 = n$ and $\sigma_1 = \sqrt{2n}$. This means

that the joint test-statistic gives a $2\sigma_N$ measurement in the mass difference as

$$N\alpha\,(\Delta m)^2_{2\sigma_N} = Nn + 2\sqrt{2Nn} \tag{A3}$$

while that for an individual log-likelihood has $N = 1$. Solving this for Δm gives

$$(\Delta m)_{2\sigma_N} = \sqrt{\frac{n}{\alpha} + \frac{2}{\alpha}\sqrt{\frac{2n}{N}}}\ . \tag{A4}$$

If we take the ratio of this with an individual log-likelihood measurement, we have

$$\frac{(\Delta m)_{2\sigma_N}}{(\Delta m)_{2\sigma_1}} = \sqrt{\frac{n + 2\sqrt{2n/N}}{n + 2\sqrt{2n}}}\ , \tag{A5}$$

where α has dropped out. We can use this formula to note a few things. First of all, we see that the maximum improvement in the sensitivity achievable asymptotically approaches 0 for the large number of bin n limit, independent of the number of log-likelihoods N combined in this way. Second, for $n = 50$ bins, the maximum improvement in the combined measurement sensitivity is 14.5% in the limit that the number of combined log-likelihoods, N, approaches infinity. Third, if we only combine $N = 2$ or 3 log-likelihoods, the maximum sensitivity improvement is only 4.3% and 6.2%, respectively. This is in the best case scenario where all the variables are uncorrelated and each α_{kv} is identical. In the realistic cases in this paper, the sensitivity improvement from combination is no more than a few percent.

---

[1] G. Aad et al. [ATLAS Collaboration], *Phys. Lett. B* **716**, 1 (2012) [arXiv:1207.7214]; S. Chatrchyan et al. [CMS Collaboration], Phys. Lett. B **716**, 30 (2012) [arXiv:1207.7235]; G. Aad et al. [ATLAS Collaboration], Phys. Rev. D **86**, 032003 (2012) [arXiv:1207.0319]; S. Chatrchyan et al. [CMS Collaboration], Phys. Lett. B **710**, 26 (2012) [arXiv:1202.1488]; CMS Collaboration, CMS-PAS-HIG-13-005; ATLAS Collaboration, ATLAS-CONF-2013-034.

[2] F. Zwicky, Helv. Phys. Acta **6**, 110 (1933); V. C. Rubin and W. K. Ford, Jr., Astrophys. J. **159**, 379 (1970); V. C. Rubin, N. Thonnard and W. K. Ford, Jr., Astrophys. J. **238**, 471 (1980); A. Bosma, Astron. J. **86**, 1825 (1981).

[3] E. Komatsu et al. [WMAP Collaboration], Astrophys. J. Suppl. **192**, 18 (2011) [arXiv:1001.4538].

[4] B. Fields and S. Sarkar, J. Phys. G **G33**, 1 (2006) [astro-ph/0601514].

[5] A. Refregier, Ann. Rev. Astron. Astrophys. **41**, 645 (2003) [astro-ph/0307212]; J. A. Tyson, G. P. Kochanski and I. P. Dell'Antonio, Astrophys. J. **498**, L107 (1998) [astro-ph/9801193].

[6] D. Clowe, M. Bradac, A. H. Gonzalez, M. Markevitch, S. W. Randall, C. Jones and D. Zaritsky, Astrophys. J. **648**, L109 (2006) [astro-ph/0608407].

[7] For a recent review, see e.g., J. L. Feng, Ann. Rev. Astron. Astrophys. **48**, 495 (2010) [arXiv:1003.0904], and references therein.

[8] E. Aprile et al. [XENON100 Collaboration], Phys. Rev. Lett. **109**, 181301 (2012) [arXiv:1207.5988].

[9] D. S. Akerib et al. [LUX Collaboration], Phys. Rev. Let **112**, 091303 (2014) [arXiv:1310.8214].

[10] R. Agnese et al. [SuperCDMSSoudan Collaboration], Phys. Rev. Lett. **112**, 041302 (2014) [arXiv:1309.3259].

[11] I. Hinchliffe, F. E. Paige, M. D. Shapiro, J. Soderqvist and W. Yao, Phys. Rev. D **55**, 5520 (1997) [hep-ph/9610544]; H. Bachacou, I. Hinchliffe and F. E. Paige, Phys. Rev. D **62**, 015009 (2000) [hep-ph/9907518]; B. C. anach, C. G. Lester, M. A. Parker and B. R. Webber, JHEP **0009**, 004 (2000) [hep-ph/0007009]; B. K. Gjelsten, D. J. Miller and P. Osland, JHEP **0412**, 003 (2004) [hep-ph/0410303]; B. K. Gjelsten, D. J. Miller and P. Osland, JHEP **0506**, 015 (2005) [hep-ph/0501033].

[12] H. C. Cheng, D. Engelhardt, J. F. Gunion, Z. Han and B. McElrath, Phys. Rev. Lett. **100**, 252001 (2008) [arXiv:0802.4290]; H. C. Cheng, J. F. Gunion, Z. Han, G. Marandella and B. McElrath, JHEP **0712**, 076 (2007) [arXiv:0707.0030]; M. M. Nojiri, G. Polesello and D. R. Tovey, [hep-ph/0312317]; K. Kawagoe, M. M. Nojiri and G. Polesello, Phys. Rev. D **71**, 035008 (2005) [hep-ph/0410160].

[13] C. G. Lester and D. J. Summers, Phys. Lett. B **463**, 99 (1999) [hep-ph/9906349]; A. Barr, C. Lester and P. Stephens, J. Phys. G **29**, 2343 (2003) [hep-ph/0304226]; M. M. Nojiri and M. Takeuchi, JHEP **0810**, 025 (2008) [arXiv:0802.4142]; P. Meade and M. Reece, Phys. Rev. D **74**, 015010 (2006) [hep-ph/0601124]; S. Matsumoto, M. M. Nojiri and D. Nomura, Phys. Rev. D **75**, 055006 (2007) [hep-ph/0612249]; C. Lester and A. Barr, JHEP **0712**, 102 (2007) [arXiv:0708.1028]; W. S. Cho, K. Choi, Y. G. Kim and C. B. Park, Phys. Rev. Lett. **100**, 171801 (2008) [arXiv:0709.0288]; B. Gripaios, JHEP **0802**, 053 (2008) [arXiv:0709.2740]; A. J. Barr, B. Gripaios and C. G. Lester, JHEP **0802**, 014 (2008) [arXiv:0711.4008]; W. S. Cho, K. Choi, Y. G. Kim and C. B. Park, JHEP **0802**, 035 (2008) [arXiv:0711.4526]; M. M. Nojiri,

Y. Shimizu, S. Okada and K. Kawagoe, JHEP **0806**, 035 (2008) [arXiv:0802.2412].

[14] J. Alwall, A. Freitas and O. Mattelaer, AIP Conf. Proc. **1200**, 442 (2010) [arXiv:0910.2522 [hep-ph]]; J. S. Gainer, J. Lykken, K. T. Matchev, S. Mrenna and M. Park, arXiv:1307.3546 [hep-ph].

[15] T. Han, I. -W. Kim and J. Song, Phys. Lett. B **693**, 575 (2010) [arXiv:0906.5009].

[16] T. Han, I. -W. Kim and J. Song, Phys. Rev. D **87**, no. 3, 035003 (2013) [arXiv:1206.5633]; T. Han, I. -W. Kim and J. Song, Phys. Rev. D **87**, no. 3, 035004 (2013) [arXiv:1206.5641].

[17] K. Agashe, D. Kim, M. Toharia and D. G. E. Walker, Phys. Rev. D **82**, 015007 (2010) [arXiv:1003.0899]; K. Agashe, R. Franceschini and D. Kim, [arXiv:1309.4776].

[18] T. Behnke, J. E. Brau, B. Foster, J. Fuster, M. Harrison, J. M. Paterson, M. Peskin and M. Stanitzki et al., [arXiv:1306.6327]; H. Baer, T. Barklow, K. Fujii, Y. Gao, A. Hoang, S. Kanemura, J. List and H. E. Logan et al., [arXiv:1306.6352]; T. Behnke, J. E. Brau, P. N. Burrows, J. Fuster, M. Peskin, M. Stanitzki, Y. Sugimoto and S. Yamada et al., [arXiv:1306.6329].

[19] M. Koratzinos, A. P. Blondel, R. Aleksan, O. Brunner, A. Butterworth, P. Janot, E. Jensen and J. Osborne et al., [arXiv:1305.6498]; M. Bicer, H. Duran Yildiz, I. Yildiz, G. Coignet, M. Delmastro, T. Alexopoulos, C. Grojean and S. Antusch et al., [arXiv:1308.6176].

[20] E. Accomando et al. [CLIC Physics Working Group Collaboration], [hep-ph/0412251]; L. Linssen, A. Miyamoto, M. Stanitzki and H. Weerts, [arXiv:1202.5940].

[21] C. M. Ankenbrandt, M. Atac, B. Autin, V. I. Balbekov, V. D. Barger, O. Benary, J. S. Berg and M. S. Berger et al., Phys. Rev. ST Accel. Beams **2**, 081001 (1999) [physics/9901022].

[22] H. U. Martyn, [hep-ph/0408226], and references therein.

[23] P. Konar, K. Kong, K. T. Matchev and M. Perelstein, New J. Phys. **11**, 105004 (2009) [arXiv:0902.2000]; J. A. Conley, H. K. Dreiner and P. Wienemann, Phys. Rev. D **83**, 055018 (2011) [arXiv:1012.1035]; Y. J. Chae and M. Perelstein, JHEP **1305**, 138 (2013) [arXiv:1211.4008].

[24] G. Aarons et al. [ILC Collaboration Design Report], arXiv:0709.1893 [hep-ph]; A. Freitas, D. J. Miller and P. M. Zerwas, Eur. Phys. J. C **21**, 361 (2001) [hep-ph/0106198]; A. Freitas, A. von Manteuffel and P. M. Zerwas, Eur. Phys. J. C **34**, 487 (2004) [hep-ph/0310182].

[25] N. D. Christensen and D. Salmon, Phys. Rev. D **90**, 014025 (2014) [arXiv:1311.6465 [hep-ph]].

[26] G. Aad *et al.* [ATLAS Collaboration], JHEP **1405**, 071 (2014) [arXiv:1403.5294 [hep-ex]];

V. Khachatryan *et al.* [CMS Collaboration], arXiv:1405.7570 [hep-ex].

[27] The ATLAS collaboration, ATLAS-CONF-2013-093; G. Aad *et al.* [ATLAS Collaboration], JHEP **1405**, 071 (2014) [arXiv:1403.5294 [hep-ex]]; CMS Collaboration [CMS Collaboration], CMS-PAS-SUS-13-017; V. Khachatryan *et al.* [CMS Collaboration], arXiv:1405.7570 [hep-ex].

[28] For a phenomenological overview, see, e.g., T. Han, S. Padhi and S. Su, Phys. Rev. D **88**, 115010 (2013) [arXiv:1309.5966 [hep-ph]].

[29] J. Kalinowski, W. Kilian, J. Reuter, T. Robens and K. Rolbiecki, JHEP **0810**, 090 (2008) [arXiv:0809.3997 [hep-ph]].

[30] T. Abe et al. [American Linear Collider Working Group], [hep-ex/0106055]; R. Blankenbecler and S. D. Drell, Phys. Rev. D **36**, 277 (1987); M. Bell and J. S. Bell, Part. Accel. **22** (1988) 301.

[31] W. Kilian, T. Ohl and J. Reuter, Eur. Phys. J. C **71**, 1742 (2011) [arXiv:0708.4233].

[32] A. Belyaev, N. D. Christensen and A. Pukhov, Comput. Phys. Commun. **184**, 1729 (2013) [arXiv:1207.6082].

[33] K. Hagiwara, R. D. Peccei, D. Zeppenfeld and K. Hikasa, Nucl. Phys. B **282**, 253 (1987).

[34] A. Birkedal, K. Matchev and M. Perelstein, Phys. Rev. D **70**, 077701 (2004) [hep-ph/0403004].

[35] E. A. Baltz, M. Battaglia, M. E. Peskin and T. Wizansky, Phys. Rev. D **74**, 103521 (2006) [hep-ph/0602187], and references therein.

[36] M. Berggren, arXiv:1203.0217 [physics.ins-det].